TBRS-associated *DNMT3A* mutations disrupt cortical interneuron differentiation and neuronal networks

Gareth Chapman[1#], Julianna Determan[1#], John R. Edwards[2], James E. Huettner[3], Sydney Crump[1], Haley Jetter[1], Harrison W. Gabel[4], and Kristen L. Kroll[1]*

[1]Department of Developmental Biology, Washington University School of Medicine, St. Louis, MO 63110

[2]Department of Medicine, Division of Oncology, Washington University School of Medicine, St. Louis, MO 63110

[3]Department of Cell Biology & Physiology, Washington University School of Medicine, St. Louis, MO 63110

[4]Department of Neuroscience, Washington University School of Medicine, St. Louis, MO 63110

[#]Equal contribution

[*]Corresponding author

Abstract

Pathogenic *DNMT3A* mutations cause Tatton-Brown-Rahman Syndrome (TBRS), a disorder characterized by intellectual disability and overgrowth of multiple somatic tissues including the brain. However, the functions of DNMT3A during human cortical development remain poorly understood. Here, we utilized newly developed human pluripotent stem cell models of TBRS-associated *DNMT3A* mutation to define DNMT3A requirements and consequences of mutation during human cortical neuron development. Profiling changes to epigenetic gene regulation across both GABAergic and glutamatergic neuron development, we identified GABAergic cortical interneurons as particularly sensitive to TBRS-associated mutation. During GABAergic neuron development, TBRS-associated DNMT3A mutations resulted in reduced DNA methylation and were associated with concomitant de-repression of gene expression, causing precocious neuronal differentiation. By contrast, the consequences of *DNMT3A* mutation on glutamatergic neuron development were less pronounced, due in part to compensatory repressive histone methylation, and resulted in increased expression of early neurodevelopmental genes during glutamatergic

neuron differentiation. Assessing the consequences of these molecular phenotypes by patch-clamp electrophysiology, we found that DNMT3A deficient GABAergic neurons were hyperactive, while glutamatergic neuron function was largely unaffected by these DNMT3A loss of function mutations. Finally, we used both low density and high density multi electrode array techniques in conjunction with glutamatergic-GABAergic neuron co-cultures to assess how TBRS-associated GABAergic neuron hyperactivity affected the emergence and development of neuronal networks. We found that TBRS GABAergic neuron hyperactivity was sufficient to drive abnormal neuronal network development, increasing the neuronal activity consolidated into neuronal bursting and networks. Ultimately, this work elucidated new roles for DNMT3A-mediated repression in human cortical development, identifying critical requirements in regulating neuronal and synaptic gene expression during GABAergic differentiation, with these TBRS-associated molecular changes driving alterations of neuronal network function likely to contribute to TBRS etiology.

Introduction

Development of the mammalian brain involves precise temporal and spatial control of gene expression and human-specific regulatory programs and features[1-4]. In particular, development of GABAergic interneurons in the cerebral cortex is a highly regulated, protracted, and multi-step process encompassing much of human gestation[5-7]. Interestingly, while the majority of cortical neurons are glutamatergic, a minority population (20-30%) of GABAergic interneurons provide essential inhibitory activity to balance neuronal excitation, which is essential for establishment and maturation of synchronized neuronal networks underlying normal brain function[8-10].

Epigenetic regulatory proteins that alter DNA and chromatin structure play key roles in transcriptional regulation during neurodevelopment[11-13]. Recent advances in clinical genome sequencing identified mutations in genes encoding several of these proteins as contributors to related syndromes characterized by brain overgrowth and intellectual disability (OGID)[14]. Among these, mutations in the *de novo* DNA methyltransferase *DNMT3A* cause Tatton-Brown-Rahman Syndrome (TBRS), a neurodevelopmental disorder involving autism spectrum disorder (ASD), brain overgrowth, craniofacial abnormalities, and intellectual disability (ID)[15-20]. Prior studies demonstrated that several TBRS-associated mutations cause distinct levels of DNMT3A loss of function (LOF)[19], with TBRS patients typically carrying heterozygous missense mutations in functional domains of *DNMT3A*, while frameshift, stop-gain, and heterozygous gene deletions appear more rarely[17].

TBRS etiology has been characterized in mouse models, highlighting anatomical and behavioral deficits associated with TBRS-contributory mutations[19,21]. These studies correlated the severity of molecular and behavioral phenotypes with levels of LOF resulting from specific *DNMT3A* mutations but did not recapitulate the brain overgrowth characteristic of TBRS patients[19,21]. Furthermore, as murine TBRS modeling efforts have focused on postnatal development, consequences of pathogenic *DNMT3A* mutation for prenatal neurodevelopment and TBRS etiology have yet to be defined. Therefore, it remains critical to assess *DNMT3A* requirements for human neurodevelopment and determine how potentially human-specific mechanisms may contribute to TBRS etiology.

Here we derived new pluripotent stem cell (hPSC) models of TBRS-associated mutation and assessed how these alter key aspects of human cortical development. We found that TBRS-associated *DNMT3A* mutations caused neural progenitor growth and differentiation abnormalities specific to GABAergic neuron development, in part due to reduced DNA

methylation and associated de-repression of neuronal differentiation- and maturation-related gene expression. While the severity of these phenotypes was proportional to extent of DNMT3A LOF, we identified a core TBRS molecular signature altered across multiple mutations and time points during GABAergic neuron development. Ultimately, this disrupted GABAergic neuron activity, directly perturbing neuronal network formation and function. Together, this work identified new DNMT3A requirements for human neurodevelopment and demonstrated that GABAergic neurons are particularly sensitive to developmental disruption by TBRS-associated mutation, providing insight into altered gene regulatory controls underlying TBRS etiology.

Methods

hPSC Model Generation and Culture

Work with hPSCs was performed in approval and accordance with the Washington University Embryonic Stem Cell Research Oversight Committee (ESCRO) under protocol #12-002. DNMT3A R882H iPSCs were reprogrammed from a male patient carrying a heterozygous dominant negative R882H (c.2922G>A) mutation and corrected using CRISPR-Cas9-based genome engineering. Whole genome sequencing was performed on both the R882H and subsequently corrected control (C-WT) iPSC lines, with summary data in Supplementary Table 15 and full data available from dbGaP (PHS000159). The pluripotency of both the R882H and C-WT iPSC lines were confirmed by assessing markers of the three primordial germ layers in teratomas generated by injecting iPSCs into the mouse fat pad. The heterozygous P904L (c.2711C>T) mutation was modelled by heterozygous introduction of the mutation into H1 human embryonic stem cells (hESCs) using CRISPR Cas9.

DNMT3A CRISPRi lines were created by transducing H1 hESCs with a single vector (Lenti-(BB)-EF1a-KRAB-dCas9-P2A-BlastR) carrying expression cassettes for both dCas9-KRAB and each gRNA. gRNAs (Supplementary Table 16) designed to target the DNMT3A promoter were identified from the Dolcetto library of gRNAs[22] and cloned into Lenti-(BB)-EF1a-KRAB-dCas9-P2A-BlastR using BsmBI (NEB). Cell lines used to produce induced glutamatergic-like neurons were generated by transducing cell lines with lentivirus carrying pLVX-UbC-rtTA-Ngn2:2A:EGFP. Transduction of hESCs was aided by the addition of 5 µg/mL polybrene (Sigma-Aldrich) immediately before addition of lentivirus. Cells recovered for 48 hours before selection (500 ng/mL puromycin or 1 µg/mL blasticidin) was applied. Once cells were selected, they were maintained under selection for the duration of subsequent experiments.

All hPSC models were maintained under feeder-free conditions on vitronectin in StemFlex Medium and cultured in an incubator with 5% CO2 at 37°C throughout all experiments. Experiments were carried out between passages 20-50 for all hPSC lines and lines periodically tested as negative for mycoplasma contamination.

Modelling cortical GABAergic and glutamatergic neuron development

Modeling of cortical GABAergic neuron development was carried out as previously described[5] (for full details, see Supplementary Material) by specifying hPSCs as medial ganglionic eminence (MGE)-like progenitors with a ventral telencephalic progenitor (V-NPCs)

character and differentiating V-NPCs into immature GABAergic cortical interneurons (V-INs). Cells were collected on day 15 of differentiation as V-NPCs and on day 35 of differentiation as V-INs. Further maturation of V-INs was performed for functional assessments as described below.

Modeling of cortical glutamatergic neuron development was carried out as previously described[23] (for full details, see Supplementary Material) with minor modifications by specifying hPSCs as subventricular zone-like progenitors with a dorsal telencephalic progenitor (D-NPCs) character and differentiating these D-NPCs into immature glutamatergic neurons (D-INs). Cells were collected on day 20 of differentiation as D-NPCs and on day 40 of differentiation as immature D-INs. Further maturation of D-INs was performed for functional assessments as described below.

Finally, induced glutamatergic-like neurons were generated as previously described[24] (for full details see Supplementary Material) by inducing overexpression of Neurogenin-2 (NGN2). Cells were considered iGluts after 14 days of differentiation.

Immunocytochemistry

Cells were fixed in 4% Paraformaldehyde (Sigma-Aldrich) before blocking in 5% donkey serum and 0.1% Tween20. Primary antibodies (Supplementary Table 17) were added overnight at 4°C. Cells were washed and incubated with secondary antibodies (Supplementary Table 17) for 1 hour at room temperature. Cells were counterstained and mounted using ProLong™ Glass Antifade Mountant with NucBlue™ Stain. Images were obtained using a custom-built spinning disc confocal from Intelligent Imaging Innovations (3i) equipped with a phasor for precise photomanipulation and image processing with ImageJ. Quantification was performed using a minimum of 3 random images taken from 3 independent biological replicate experiments using CellProfiler[25], requiring a minimum of 60% overlap between immunofluorescence signal and DAPI staining for co-localization to be scored.

RNA-Seq

RNA was isolated and sequenced to a depth of ~30 million (M) reads per sample by the Washington University Genome Technology Access Center at McDonnell Genome Institute (GTAC@MGI). After quality control and quantification differential gene expression analysis was performed using DESeq2 with raw results available from GEO under accession GSE294189 (for full details see Supplementary Material).

Whole Genome Bisulfite Sequencing (WGBS)

DNA was isolated and bisulfite converted with libraries pooled and sequenced at Washington University GTAC@MGI. Sequences were trimmed for quality and then aligned, with methylation data at individual cytosines extracted and differentially methylated regions identified (for full details, see Supplementary Material). All raw and processed data is available from dbGaP (in process) or GEO (GSE294191).

CUT&Tag

CUT&Tag was performed on all samples as previously described[5] (for full details see Supplementary Material). Analysis of differential levels of histone mark occupancy was performed using DiffBind[26] with complete result tables for significant changes presented as Supplementary Tables. All raw and processed data is available from GEO (GSE294186).

Reverse Transcription and Quantitative PCR (RT-qPCR)

RNA was isolated using the NucleoSpin RNA kit, with ≥1 µg used to make cDNA using the High-Capacity cDNA Reverse Transcription Kit. Equal quantities of cDNA were used as template for quantitative PCR (qPCR), using the Applied Biosystem StepOne Plus quantitative PCR system. GAPDH was used as an endogenous quantitative control and all primers used can be found in Supplementary Table 18. Data was generated from a minimum of 3 biological replicate samples, each of which consisted of 3 technical replicates. All statistics were performed using abundance relative to endogenous control, and data presented as fold change by comparison with appropriate control.

Western Blotting

Protein was isolated in RIPA buffer with Halt™ Protease and Phosphatase Inhibitor Cocktail and western blotted using Bolt™ 4 to 12%, Bis-Tris, 1.5 mm, Mini Protein Gels and then transferred to 0.2 µm nitrocellulose membrane. Nonspecific antibody binding was blocked by 5% milk solution, and primary antibodies (Supplementary Table 17) were incubated with free floating membranes overnight at 4°C. Secondary antibodies were HRP conjugated Goat anti-Rabbit IgG and Goat anti-Mouse IgG, each used at a 1:10,000 dilution. Visualization was performed by chemiluminescence using SuperSignal™ West Pico PLUS Chemiluminescent Substrate, all band intensities were normalized to GAPDH loading controls, and a minimum of

3 biological replicates were averaged before statistical analysis. Statistical analysis was performed on normalized signal intensity, with data presented as fold change compared to appropriate controls.

Sphere Size and Outgrowth Measurements

Images were taken from D12 of differentiation, using a 4x objective, for 20 neurospheres per biological replicate across a minimum of 3 biological replicates per condition. Sphere size and outgrowth were measured using ImageJ and outgrowth is defined as the area of cells outgrown from the plated neurosphere ,normalized to corresponding sphere size.

Electrophysiology

D28 D-INs and D23 V-INs were plated on rat cortical astrocytes and matured until D60, before electrophysiological measurements were taken as described previously[27] (for full details see Supplementary Material). Results were analyzed using non-parametric rank sum tests comparing TBRS models to matched isogenic controls with raw results presented in Supplementary Tables.

Multi-Electrode Array Recordings

All low-density multi-electrode array (MEA) experiments were performed using CytoView MEA 48-well plates. Co-cultures of matured D-INs and V-INs (at a 70:30 ratio) were plated onto MEAs after 50 days of differentiation (for full details see Supplementary Material). Electrophysiological activity was recorded every 5 days using hardware (Maestro Edge) and software (AxIS 1.5.2) from Axion Biosystems (for full details see Supplementary Material). Analysis was carried out using Axion built-in neural metric analysis tool with synchronized bursts (SBs) identified using an envelope algorithm, defining a SB by identifying periods when activity exceeds a threshold of 1 x standard deviation above the mean with a minimum of 200ms between SBs and at least 35% of electrodes included. A minimum of 4 MEAs per cell line per differentiation (technical replicates) have been considered for the analysis with a minimum of 3 separate differentiations used per time point.

All high-density MEA experiments were performed using CorePlate™ 6W 38/60 MEAs. Co-cultures of V-INs and iGluts (at a 30:70 ratio) were plated onto MEAs alongside rat astrocytes (for full details see Supplementary Material). Electrophysiological activity was

recorded on D50 and D82 of V-IN differentiation, using the HyperCAM Alpha system (3Brain) and accompanying BrainWave5 software (for full details see Supplementary Material). Analysis was conducted using BrainWave5 software identifying an electrode burst using an inter-spike-interval (ISI) algorithm, as a period with a minimum of 10 spikes separated by a maximum ISI of 70 ms and defining a bursting electrode as one with at least 2 bursts in a 10-minute recording. Finally neuronal network bursting was defined using a recruitment-based algorithm with a minimum threshold of 0.1 spikes/s across a minimum of 30% of active electrodes, using a 150 ms bin size, and requiring a 100-spike minimum. All active electrodes (spiking rate > 0.1 Hz) were included in the analysis of neuronal and neuronal network activity unless otherwise stated. For each condition 3 MEAs were plated with the same MEAs recorded longitudinally.

Quantification and Statistical Analysis

Where appropriate, statistical analysis was carried out using GraphPad Prism version 9 (GraphPad Software; La Jolla, CA, USA, available from www.graphpad.com) and/or RStudio version 3.5.1 (RStudio: Integrated development environment for R; Boston, MA, USA. Available from www.rstudio.org). All technical replicates were averaged before statistical analysis and statistical tests used for each data analysis are detailed in the figure legends or in method details section for specific analysis paradigms. A minimum of 3 independent differentiations were used for each time point or biological condition with the number of differentiations used for each sample listed in figure legends as n. The results in figures are presented as group mean +/- standard error (SE) indicating each biological replicate used for the analysis, unless otherwise specified in figure legends. Statistical significance is indicated as follows: n.s., not significant; $*$, $p < 0.05$; $**$, $p < 0.01$; $***$, $p < 0.001$; $****$, $p < 0.0001$ unless otherwise specified in figure legends.

Results

Pathogenic *DNMT3A* mutation causes a precocious, dose-dependent increase in neuronal gene expression in neural progenitors

To elucidate the consequences of pathogenic *DNMT3A* mutations on human neurodevelopment, we characterized hPSC models carrying heterozygous R882H or P904L TBRS mutation (Fig. 1a-b), which cause ~80% and ~50% loss of function (LOF), respectively[21,28]. These models were compared to paired isogenic controls (C-WT/WT; Fig. 1a-b). Using our established methods[5,23,27,29], we derived neuronal progenitors with dorsal (D-NPC, Fig. 1c) or ventral (V-NPC, Fig. 1d) telencephalic character from these models; these give rise to cortical glutamatergic and GABAergic neurons, respectively. We initially assessed altered proliferation in R882H NPCs, observing a V-NPC-specific increase in neurosphere outgrowth versus controls (Fig 1e, Supplementary Fig. 1a). R882H V-NPCs, but not D-NPCs, also exhibited an increased fraction of Ki-67-immunopositive proliferating progenitors, suggesting that increased sphere overgrowth involved increased V-NPC proliferation (Fig. 1f, Supplementary Fig. 1b). We next examined transcriptomic differences by RNA-sequencing, finding significant differences between R882H and control V-NPCs (Supplementary Fig. 1c), while D-NPC comparisons showed less distinction (Supplementary Fig. 1d). Correspondingly, the R882H and control V-NPC comparison revealed greater numbers of differentially expressed genes (DEGs) versus parallel D-NPC comparisons (1,314 versus 247, respectively; Supplementary Table 1).

Focusing on the V-NPCs, a majority of DEGs (~68%) were upregulated in R882H V-NPCs versus controls (Supplementary Fig. 1e, Supplementary Table 1), while these genes were enriched for neuronal maturation- and function-associated gene ontology (GO) terms (Supplementary Fig. 1f, Supplementary Table 2). We hypothesized that R882H V-NPCs might be precociously differentiating into immature GABAergic interneurons (V-INs) and thus next compared gene expression in control and R882H V-NPCs with control V-INs. However, this comparison revealed that R882H V-NPCs retained V-NPC identity (Supplementary Fig. 1g), with most genes that were up-regulated in R882H versus control V-NPCs (~70%) were instead downregulated in R882H V-NPC versus WT V-IN comparisons (Supplementary Table 1). These data suggest that, while TBRS-associated DNMT3A LOF increased neuronal gene expression in progenitors, this was insufficient to trigger spontaneous neuronal differentiation.

Assessing whether a similar phenomenon occurred in P904L V-NPCs, we found that both TBRS model V-NPCs were similarly distinct from their isogenic controls (Supplementary Fig.

1h), while most DEGs common to both TBRS models (~75%; 'TBRS-shared' DEGs) were upregulated (Supplementary Table 1) and involved in neuronal differentiation and maturation (Fig. 1g, Supplementary Table 2). More upregulated DEGs were defined in R882H-control than P904L-control V-NPC comparisons (890 versus 459, Fig. 1h, Supplementary Table 1), while TBRS-shared DEGs also showed greater effect sizes in R882H-control V-NPC comparisons (Supplementary Fig. 1i). These data support a stronger effect of R882H versus P904L on gene expression, consistent with their relative LOF effect[21,28].

To further examine the dose dependency of DNMT3A LOF-associated increases in both cell proliferation and neuronal gene expression, we generated CRISPRi DNMT3A deficiency models (G1/G2, Fig. 1i), each of which significantly reduced DNMT3A mRNA (Fig. 1j) and protein levels (Fig. 1k). Like our TBRS mutant models, both CRISPRi deficiency models exhibited increased relative progenitor sphere outgrowth (Fig. 1l) and proliferating cell fractions (Fig. 1m), with phenotype severity correlating with extent of LOF (Fig. 1j-k; ~25% and ~50% for G1/2, respectively). We also used RT-qPCR across TBRS and CRISPRi V-NPCs to assess the expression of 30 genes that were upregulated in both TBRS models, exhibited greater effect size in R882H versus P904L V-NPCs and were associated with specific GO terms (Fig. 1n, Supplementary Table 1-2). These data consistently demonstrated the greatest differential expression between R882H and its isogenic control, while the P904L-control and G2 model-control comparisons exhibited intermediate effects, and G1-control comparisons showed the most modest effects (Fig. 1n). These findings indicate that dose-dependent DNMT3A LOF drives both abnormal overgrowth and precocious onset of neuronal gene expression in neural progenitors.

DNMT3A directly restrains the onset of neuronal gene expression in ventral telencephalic progenitors

To investigate the proximal cause of precocious neuronal gene expression in TBRS V-NPCs, we assessed changes in DNA methylation by whole genome bisulfite sequencing (WGBS-seq). We observed mild (~2%) but significant reduction of global CpG methylation (mCG) specific to R882H V-NPCs (Fig. 2a, Supplementary Fig. 2a), with CpG islands and shores exhibiting greater mCG reduction than shelves or gene bodies (Fig. 2a). Analyzing differentially methylated regions (DMRs) in V-NPCs defined 67,192 DMRs, 87% of which had higher mCG in control versus R882H V-NPCs (hypoDMRs, Fig. 2b, Supplementary Table 3). These effects were consistent with DNMT3A LOF and were further supported by the greater

hypoDMR effect size relative to hyper-methylated regions (hyperDMRs, Supplementary Fig. 2b). Similar analysis in D-NPCs identified 57,724 DMRs, of which ~70% were R882H hypoDMRs (Supplementary Table 3), while both hypo- and hyperDMRs showed similar mCG level fold differences in R882H-control comparisons (Supplementary Fig. 1c). In further analysis, both hypoDMRs and hyperDMRs were enriched at key regions of interest (ROI) for DNA methylation relative to randomly resampled DMRs (Fig. 2c), with hypoDMRs often found in proximity to promotors (Supplementary Fig 2d). Correlating hypoDMRs with transcriptomic differences in R882H V-NPCs, promoter-hypoDMRs were associated with greater changes in differential gene expression, relative both to all and gene body hypoDMRs, a relationship specific to hypoDMRs (Fig. 2d). Correlating these promotor-hypo-DMRs with DEGs up-regulated in R882H V-NPCs, we identified enrichment for a set of genes involved in neuronal maturation and terminal neuronal differentiation (Fig. 2e-f, Supplementary Table 4). Together, these results indicate that promotor-hypoDMRs are associated with significant dysregulation of neuronal gene expression programs in R882H V-NPCs.

Performing a similar analysis in P904L V-NPCs, we found no significant global mCG changes but defined 55,308 DMRs; 67% of these were hypoDMRs (Supplementary Table 3), with both hypo- and hyperDMRs showing similar effect sizes (Supplementary Fig. 2e). Similar to DMRs in R882H V-NPCs, both P904L V-NPC hypo- and hyperDMRs were enriched at all ROIs examined (Supplementary Fig. 2f) with both subsets of DMRs often located near promotors (Supplementary Fig 2g). We identified 7,720 'TBRS-shared' DMRs present in V-NPCs in both models, with R882H exhibiting a greater loss of mCG than P904L at these sites (Fig. 2g; all DMRs). However, the DMRs that were hypo-methylated in both models showed similar mCG reduction across models (Fig. 2g; Both-Hypo), while R882H-specific hypoDMRs showed less mCG reduction in the P904L model (Fig. 2g; 882-Hypo). In further analysis, both TBRS-shared hypo- and hyperDMRs were particularly enriched at promotors (Supplementary Fig. 2h) and were associated with neuronal differentiation-related genes (Fig. 2h, Supplementary Table 4). Of the genes associated with TBRS-shared DMRs, 228 were also TBRS-shared DEGs; notably, this DEG subset was independently enriched for neuronal differentiation-related GO terms (Supplementary Table 4). Together, these data demonstrate that TBRS-associated loss of DNA methylation causes precocious neuronal gene expression in V-NPCs, suggesting that DNMT3A may have a significant role in controlling V-NPC differentiation into V-INs.

Increased repressive histone methylation compensates for loss of DNA methylation to restrain neuronal gene expression in TBRS neural progenitors

Recent work has demonstrated a role for EZH2 in controlling neuronal maturation[30], while pathogenic *EZH2* mutations cause an OGID syndrome similar to TBRS[14,31-33]. Therefore, we investigated whether levels of histone H3 lysine 27 tri-methylation (H3K27me3), deposited by EZH2, were also altered by TBRS-associated loss of DNMT3A function. Interestingly, intersecting R882H DMRs in V-NPCs with our previously published histone modification state data for wildtype V-NPCs (H3K4me3/K27ac/K27me3/K9me3 enrichment[5]) revealed H3K27me3 enrichment at R882H hypoDMRs (Supplementary Fig. 3a). Furthermore, most hypoDMR sites enriched for H3K27me3 signal lost this mark during V-NPC-neuronal differentiation (Fig. 3a), while another repressive histone modification (H3K9me3) did not exhibit this trend (Supplementary Fig. 3b). Therefore, we assessed a potential relationship between TBRS-associated loss of DNA methylation and increased H3K27me3, beginning by profiling differential H3K27me3 enrichment in R882H versus control V-NPCs. This analysis identified 6,439 regions with differential H3K27me3 signal (DKS), 58% of which exhibited increased H3K27me3 enrichment in R882H V-NPCs ('hyperDKS', Fig. 3b, Supplementary Table 5). Intersecting these R882H DKSs with R882H DMRs, we found that a majority of hyperDKSs intersected with hypoDMRs (~62%), while DKSs rarely associated with hyperDMRs (Fig 3c). By contrast, performing similar analyses in the P904L model identified relatively few DKSs (Supplementary Table 5) and little overlap between P904L hyperDKSs and hypoDMRs. From these data, we concluded that the more severe loss of DNA methylation in the R882H V-NPCs might trigger an R882H-specific compensatory increase in H3K27me3 enrichment at hypoDMRs.

We further examined the potential relationship between increased H3K27me3 and altered gene expression, finding that most R882H hypoDMRs and hyperDKSs (77%) associated not with R882H V-NPC DEGs, which were predominantly neuronal, but instead with genes involved in early neuro-epithelium development (Fig. 3d, Supplementary Table 6). This suggested that, while this compensatory regulatory mechanism can normalize repression of early neuroepithelial gene expression in V-NPCs, it remains insufficient to correct all TBRS-associated gene dysregulation. This was of interest because, while both R882H V-NPCs and D-NPCs exhibit significant losses of DNA methylation, in D-NPCs this resulted in minimal gene expression changes. Based on these data, we hypothesized that compensatory

H3K27me3-mediated repression could account for regulatory decoupling, such that mCG loss did not cause dysregulated D-NPC expression. To test this, we examined H3K27me3 changes in R882H versus control D-NPCs, identifying 3,757 DKSs (Supplementary Table 5), 59% of which were hyperDKSs (Fig. 3e). Reminiscent of our findings above, the majority (55%) of these hyperDKSs overlapped with R882H hypoDMRs (Supplementary Table 3), while <5% of these sites were associated with an R882H DEG in D-NPCs (Supplementary Table 1).

We next compared these phenomena across NPC types, defining 674 genes associated with a hyperDKS and hypoDMR in both V- and D-NPCs. Many of these genes were most highly expressed in either wildtype hPSCs or post-mitotic neurons and were involved in 'cell fate commitment' and 'channel activity', respectively (Fig. 3f-g, Supplementary Table 6). From these data, we hypothesized that increased H3K27me3 in TBRS models might normalize expression of these genes. To test this, we treated TBRS and control D-NPCs with an EZH2 inhibitor, thus blocking H3K27me3 deposition, and assessed the expression of 15 of the aforementioned genes, including 9 hPSC-specific (e.g. ESRG, Fig. 3h-i) and 6 neuronal genes (e.g. ARX, Fig. 3h-i). EZH2 inhibition significantly increased expression of all 15 genes in the R882H but not P904L D-NPCs (Fig. 3j, Supplementary Fig 3c). Therefore, these data support the conclusion that increased H3K27me3 compensates for a more severe loss of mCG in the R882H model. We suggest that this mechanism could account for the relatively limited gene expression changes that result from R882H mutation in D-NPCs, while being insufficient to counteract the upregulation of neuronal gene expression resulting from loss of DNA methylation in R882H V-NPCs.

TBRS mutations cause precocious synaptic gene expression in immature GABAergic neurons

We next investigated whether the precocious neuronal gene expression found in TBRS V-NPCs persisted as V-NPCs differentiated into immature GABAergic neurons (V-INs, Fig. 4a). As in our prior NPC analysis, greater transcriptomic differences were identified in R882H-control versus P904L-control V-IN comparisons (Fig. 4b). Specifically, we identified 2,269 DEGs in R882H V-INs, ~73% of which were upregulated (Supplementary Table 7) and these were enriched for 'synapse' related genes (Fig. 4c, Supplementary Table 8). While fewer DEGs were identified in P904L V-INs (687), a similar proportion (~70%) were upregulated (Supplementary Table 7) and we defined 247 V-IN TBRS-shared DEGs (Supplementary Table 7); these were again enriched for 'synapse'-related genes (Fig. 4d, Supplementary Table 8).

Focusing on TBRS-shared DEGs in V-INs, and reminiscent of our findings for V-NPCs, we found larger effect sizes in R882H-control versus P904L-control comparisons; this relationship was particularly striking when examining the 42 synapse-associated TBRS-shared DEGs, 41 of which showed greater effect size in R882H V-INs (Fig. 4e, Supplementary Table 7).

Assessing DNA-methylation changes in R882H V-INs, we observed a trend towards global mCG reduction that did not reach significance, while there were significant mCG losses at CpG islands, shores and TSSs, similar to our findings in V-NPCs (Fig. 4f). We identified 89,060 DMRs in R882H V-INs, of which ~88% were hypoDMRs, exhibiting an average ~20% mCG reduction (Supplementary Fig. 4a, Supplementary Data 9). Furthermore, while both R882H V-IN hypo- and hyperDMRs were enriched at key ROIs (Supplementary Fig. 4b), hypoDMRs were more frequently located at promotors than hyperDMRs (Supplementary Fig. 4c). A similar analysis in P904L V-INs showed more subtle trends in mCG reduction relative to R882H, with no significant difference in overall mCG levels globally or across key ROIs (Supplementary Fig. 4d). However, we did identify 30,818 P904L DMRs, 70% of which were hypoDMRs with an average ~14% mCG reduction (Supplementary Fig. 4e). Comparing mCG changes between TBRS models in V-INs, we found that hypoDMRs called in the R882H model were reduced or absent in P904L V-INs, while P904L-called hypoDMRs instead exhibited modest but significant mCG reduction in R882H V-INs, and DMRs common across models ('TBRS-shared') exhibited similar mCG changes in both models, with larger effect sizes in R882H V-INs (Fig. 4g, Supplementary Table 9). Correlating TBRS-shared hypoDMRs with TBRS-shared DEGs in V-INs revealed an enrichment for synaptic genes, as seen previously for V-NPCs (example Fig. 4h, Supplementary Table 8). Further comparing mCG differences between TBRS model V-NPCs and V-INs highlighted a phenomenon whereby R882H hypoDMRs persisted through the differentiation of V-NPCs into V-INs, while P904L hypoDMRs were instead timepoint-specific (Supplementary Fig. 3f-g,), a finding replicated by an examination of TBRS-shared hypoDMRs (Fig 4i, Supplementary Table 9). Together, these findings provided further evidence that *DNMT3A* LOF mutations cause upregulation of synaptic genes due to concomitant loss of DNA methylation, while the severity and persistence of these phenotypes is proportional to the extent of LOF resulting from the specific TBRS-associated mutation. Ultimately, these findings support a critical role for DNMT3A-mediated repressive DNA methylation to restrain precocious neuronal and synaptic gene expression during GABAergic neuron differentiation and maturation.

DNMT3A regulates the silencing of early neurodevelopmental gene expression programs in glutamatergic neurons

Given the persistent effect of TBRS-associated loss of DNMT3A function during GABAergic neuron differentiation, we also wished to assess whether, despite minimal effects on D-NPC specification, TBRS-associated mutations might alter subsequent D-NPC differentiation into immature glutamatergic neurons (D-INs, Fig. 5a). Assessing transcriptomic changes across TBRS D-INs versus controls revealed significant transcriptomic differences across models (Fig. 5b) and defined TBRS-shared up-regulated DEGs (Fig. 5c, Supplementary Table 10). However, unlike our findings for V-INs, these DEGs were enriched for genes involved in early neural cell specification (Fig. 5d, Supplementary Table 11), while a majority of DEGs were normally highly expressed in control hPSCs or D-NPCs (Fig. 5e). These data suggested that, during D-IN differentiation, DNMT3A LOF might disrupt the downregulation of early neurodevelopmental gene expression programs.

To assess whether this phenomenon could involve earlier alteration of D-NPC specification, we performed similar analyses during hPSC reprogramming to glutamatergic-like neurons (iGluts) by transcription factor overexpression, a process that bypasses NPC generation (Fig. 5f). TBRS iGluts showed distinct transcriptomic changes by comparison with TBRS D-INs (Fig. 5g) and few (128) TBRS-shared DEGs were identified, despite relatively larger numbers of R882H or P904L mutation-specific DEGs (852 and 783 respectively, Supplementary Table 10). Further analysis also identified a contrast between findings in R882H versus R904L iGluts, with upregulated R882H iGlut DEGs enriched for early neurodevelopmental genes like TBRS D-INs (Fig. 5h, Supplementary Table 11), while DEGs up-regulated in P904L iGluts were instead enriched for synaptic genes (Fig. 5h, Supplementary Table 11).

Examining mCG changes across these TBRS models, we found global mCG reductions in both R882H D-INs and iGluts (Supplementary Fig. 5a-b) but not in P904L D-INs or iGluts (Supplementary Fig. 5c-d). In comparing hypoDMRs between these models, we found a larger number in R882H (43,296) and P904L (27,958) D-INs, relative to R882H (34,258) and P904L (10,317) iGluts (Supplementary Table 12). We further compared hypoDMRs across D-INs and iGluts, finding that ~25% of R882H D-IN hypoDMRs were also iGlut hypoDMRs, while only ~6% of P904L hypoDMRs were shared across both the D-IN and iGlut models (Supplementary Table 12). Given the lack of concordance between findings for our TBRS models in these different experimental paradigms, we further examined mCG changes between R882H and P904L iGluts, finding a large number (20,089) of hyperDMRs specific to P904L iGluts, while

35% of genes associated with a P904L iGlut hyperDMR were instead associated with an R882H iGlut hypoDMR (Supplementary Table 12). In assessing examples of these trends, we identified two genes critical for NPC maintenance (Fig. 5i, *NOTCH1* and *TGFB1*) that are associated with a P904L iGlut-specific hyperDMR. Notably, these were both associated with hypoDMRs and were up-regulated DEGs in R882H and P904L D-INs and R882H iGluts but not in P904L iGluts. Together, these data suggested that distinct compensatory increases in DNA methylation may explain the unique transcriptomic changes we observed in the P904L iGlut models, relative to the other experimental paradigms and models assessed here. Interestingly, this is reminiscent of the unique regulatory changes observed in mouse models carrying the P904L but not R882H orthologous *DNMT3A* mutation[34].

While this data suggested that DNMT3A may have a distinct role in silencing early neurodevelopmental gene expression programs during D-IN but not V-IN differentiation, we also wanted to assess if DNMT3A might also have some shared roles in both D-IN and V-IN differentiation. To test this, we refocused our analysis on shared regulatory alterations across TBRS models and differentiation paradigms, noting that the methodology used to generate neurons predominantly affected hypoDMR magnitude rather than their presence or absence (Fig. 5j). In these analyses, TBRS-shared hypoDMRs in both D-INs and iGluts were associated with synapse formation-related genes, reminiscent of our results for TBRS V-INs (Supplementary Table 11). Therefore, we assessed whether these data reflected shared mCG changes across D-INs and V-INs, finding that TBRS-shared hypoDMRs that were identified either in D-INs or V-INs showed similar mCG loss in both R882H V-INs and D-INs, while mCG changes in P904L neurons were less consistent across these neuronal cell types (Fig. 5k). Further examining TBRS-shared hypoDMRs present in both D-INs and V-INs revealed that these sites were largely at promotors (Fig 5l) of synapse-related genes (Fig 5m, Supplementary Table 11) and that, while ~10% of these genes were DEGs in R882H V-INs, <2% were DEGs in R882H D-INs (Supplementary Table 7 and 10). Together, these findings support a shared loss of DNA methylation associated with dysregulated expression of neuronal and synaptic genes across TBRS mutational models, neuronal cell types, and derivation paradigms; however, despite these shared regulatory roles, TBRS-associated loss of DNMT3A function had distinct effects on the processes of GABAergic versus glutamatergic neuron differentiation.

TBRS mutations cause GABAergic neuron hyperactivity and alter neuronal network function

We next sought to investigate the functional impact of the epigenetic disruptions caused by TBRS-associated *DNMT3A* LOF, performing patch clamp electrophysiological analysis on D-INs and V-INs matured for a further 20 days in co-culture with rat astrocytes. Consistent with our prior cellular and molecular phenotyping, electrophysiological analysis of glutamatergic neurons (D-INs matured on rat astrocytes) revealed no alteration of measures of neuronal health or function in either TBRS model (Supplementary Fig. 6a-d, Supplementary Table 14). While R882H GABAergic neurons (V-INs matured on rat astrocytes) also showed no significant changes in measures of neuronal health (Fig. 6a, Supplementary Fig. 7a-d, Supplementary Table 13) these cells showed hyperactivity upon stimulation (Fig. 6b-c), characterized by increased action potential (AP) amplitude and decreased halfwidth (Fig. 6d-e). Furthermore, assessing channel activity in R882H GABAergic neurons demonstrated increased sodium uptake, transient outward current (TOC), and GABA responsiveness (Fig. 6f-h, Supplementary Fig. 7e). Likewise, both P904L glutamatergic and GABAergic neurons showed an overall increased level of activity upon stimulation (combined data in Fig. 6i-j), while both types of neurons again showed no significant changes in measures of neuronal health (Supplementary Fig. 7i-k, Supplementary Table 13).

We next assessed TBRS-associated changes in neuronal network activity in glutamatergic and GABAergic neuron co-cultures by using low density multi-electrode arrays (LD-MEAs). These analyses demonstrated increased activity in R882H co-cultures versus controls from D60 (Fig. 7a-b), while P904L co-cultures instead showed decreased activity during the same period (Supplementary Fig. 8a). In R882H cultures, these effects were accompanied by increased network bursting frequency with no sustained changes in either inter-spike-interval (ISI) within bursts or number of spikes per burst (Fig. 7c-d, Supplementary Fig. 8b-c). P904L co-cultures instead showed an increased ISI within bursts and decreased number of network bursts, with no change in numbers of spikes per burst or network burst duration (Supplementary Fig. 8d-g).

Given these differences between the TBRS models and our molecular findings, we chose to selectively test the contribution of TBRS GABAergic neurons to network dysfunction, by comparing activities of TBRS versus control GABAergic neurons assessed in co-culture with control iGlut neurons (supplemented with rat astrocytes) on high density multi electrode arrays (HD-MEAs). Assessing these cultures at D50, we found no significant difference in mean firing

rate (Fig. 7e-f), similar to our LD-MEA results; however, we did observe increased numbers of electrodes exhibiting bursting for both TBRS models (Fig. 7e,g). Assessing the same cultures after further maturation to day 82, we found increased neuronal activity in both TBRS models, with a greater effect size in R882H (Fig. 7h-i). This finding was coupled with a decreased ISI and increased coefficient of variation (CoV) of ISI in both models, with R882H again showing a greater effect size than P904L (Supplementary Fig. 9a-b). Examining specific characteristics of the neuronal activity measured, we found no significant differences when examining all activity; however, activity that segregated into bursts showed decreases in measures of peak amplitude (Supplementary Fig. 9c-f).

In addition to the increased activity exhibited by TBRS GABAergic neurons, we also found an increased number of spikes per burst (Fig. 7j), while R882H also exhibited an increased bursting frequency (Supplementary Fig. 9g). Further, while the proportion of spikes restricted to neuronal bursts was more substantially increased in the P904L model (Supplementary Fig. 9h), both models showed similar decreases in average ISI within bursts (Fig. 7k). Finally, while we found no evidence for alterations in the overall frequency of neuronal network activity in either TBRS model (Fig. 7h,l), we observed a decrease in the duration of network bursts (Fig. 7h,m) coupled with increased numbers and proportion of spikes within network bursts across both TBRS models (Fig. 7n, Supplementary Fig. 9i); these observations were again coupled with decreased ISI and an increased ISI CoV of spikes within network bursts (Fig. 7o, Supplementary Fig. 9j). Together, these data demonstrate that TBRS-associated GABAergic neuron dysfunction caused an increase in neuronal and bursting activity that was generally more severe in the R882H model, while we also observed consistent effects on neuronal network activity, including altered organization of activity within network bursts.

Discussion

In this work, we derived new human cellular models of pathogenic *DNMT3A* mutation and used these to characterize TBRS-contributory alterations of neurodevelopment and neuronal network function. Surprisingly, we found that GABAergic neuron development was selectively sensitive to TBRS-associated DNMT3A LOF, causing substantial dysregulation of neuronal and synaptic gene expression and altered function. Differences in the relative DNMT3A LOF conferred by each TBRS-associated mutation correlated with phenotypic severity, reminiscent of the differential phenotypic severity resulting from orthologous mutations in mouse models[19,34]. Mouse bone marrow cells with heterozygous R878H mutation (orthologous to human R882H) exhibit TBRS-associated mCG alterations, reminiscent of our findings[19]; however, most subsequent assessment of methylation deficits in mouse models has focused on non-CG methylation catalyzed by DNMT3A in post-mitotic neurons, while reported mCG differences in those models were comparatively less informative[19,21,34]. Here, human TBRS models exhibited temporally specific disruptions of DNA methylation during development; these were particularly deleterious for GABAergic neuron development, as they resulted in broadly dysregulated developmental onset of neuronal and synaptic gene in both progenitors and immature neurons. Thus, while most analysis in TBRS mouse models has focused on altered DNA methylation present in adult brain[19,21,34], our findings support a requirement for DNMT3A-mediated DNA methylation disrupted by TBRS to alter the trajectory of human neuronal development, accounting for some neurodevelopmental origins of the disorder. Furthermore, while the neurodevelopmental mCG perturbations defined here may not persist into adulthood, the associated GABAergic neuron dysfunction we defined here has profound effects on the formation and function of neuronal circuitry, likely to continue through post-natal and adult stages.

Our analysis of models of early human cortical development identified TBRS-associated over-proliferation primarily in ventral telencephalic, medial ganglionic eminence-like neuronal progenitors. While reminiscent of findings for other genetic NDDs that alter neural progenitor proliferation[35-38], such progenitor over proliferation and its specificity to GABAergic neurodevelopment has not been observed in mouse TBRS models, supporting human cellular models as a useful paradigm for investigating cellular origins of brain overgrowth in OGID syndromes. Likewise, while increased progenitor proliferation is often coupled with delayed differentiation in other NDD models[35,39], here disrupted DNA methylation not only increased progenitor proliferation but also triggered precocious neuronal gene expression. Critically, both

this elevated neuronal gene expression, and the accompanying loss of DNA methylation persisted through GABAergic neuron differentiation, highlighting significant, previously undocumented DNMT3A requirements to gate the temporal onset of neuronal gene expression. Therefore, while epigenetic regulation is commonly appreciated to repress non-neuronal gene expression during neural development[40,41], these findings define a new requirement for DNA methylation-based epigenetic repression to temporally restrain neuronal differentiation onset. This has not previously been documented, although H3K27me3-mediated epigenetic gene repression was recently shown to similarly restrict neuronal maturation[30].

These results underscore imbalanced excitatory and inhibitory neuronal activity as a core driver of TBRS, reminiscent of findings for other NDDs[42-46], with GABAergic interneuron dysfunction contributing significantly to this imbalance here[47-50]. hPSC models of other NDDs including ASD[5,51,52], intellectual disability[53] and schizophrenia[54,55] have highlighted deficits in GABAergic neuron development or function associated with these disorders. However, GABAergic neuron sensitivity to TBRS mutation was not previously documented in mouse models, although DNMT3A is highly expressed in postmitotic murine GABAergic neurons[56]. Interestingly, interneuron development is also severely impaired[57] in mouse Rett syndrome models with mutation of *MECP2*, which reads out DNMT3A-deposited methylation[58-63]. Likewise, hPSC-derived Rett syndrome GABAergic neurons exhibited both increased GABA-related gene expression and neuronal excitability similar to our findings[64] and restoration of MECP2 expression selectively in GABAergic neurons in mouse brain can rescue multiple Rett syndrome-associated phenotypes[65]. Therefore, altered GABAergic neuron development may constitute an under-characterized, core contributor to TBRS and related NDDs.

GABAergic neuron function has been explored as a contributor to NDD etiology, but generally by assessment in isolated GABAergic neurons, while few studies have examined contributions of GABAergic neuron-specific dysfunction to altered neuronal network formation and function. Here, we examined how TBRS-mutant GABAergic neurons affected network function in co-cultures with control glutamatergic neurons, demonstrating that GABAergic neuron-selective mutation was sufficient to drive TBRS-associated network dysfunction. Furthermore, while electrophysiology, LD-MEA, and HD-MEA all demonstrated compatible functional alterations, the greater resolution of HD-MEA enabled more nuanced investigation of TBRS-associated network disruption. MEA technology has recently emerged as a paradigm to investigate neuronal network dysfunction. For instance, LD-MEA assessment of dysfunction in Rett Syndrome iGluts demonstrated neuronal network hyperactivity, reminiscent of our findings for TBRS[66]. However, conclusions that can be drawn from

conventional LD-MEA have often been limited by the lower volume of data acquired for each neuronal network, leading to inconsistencies across and within some NDD studies[23,37,67-75]. Here, utilizing HD-MEA to investigate cell type-specific TBRS-associated network dysfunction highlighted its ability to identify specific, robust alterations of network synchrony. For example, the higher resolution of HD-MEA enabled us to detect emergence of TBRS-associated network disruption by day 50 of neuronal differentiation, when it was not detectable by LD-MEA. This work demonstrates that HD-MEA, particularly as used here to define neuronal cell type-specific disruptions, can provide robust metrics for investigating the etiology and development of NDD-associated network dysfunction.

While this work identified multiple convergent epigenetic alterations associated with both TBRS-associated mutations, we also identified a compensatory mechanism involving increased H3K27me3 specific to R882H glutamatergic neurons. This resembles consequences of conditional DNMT3A loss in mouse excitatory neurons, which resulted in increased H3K27me3 enrichment at sites that lost DNA methylation[76]. A recent study also identified an 'epigenetic barrier' preventing premature neuronal maturation and demonstrated that EZH2-mediated H3K27me3 deposition underlies this phenomenon[30]; together, these findings underscore a critical role for H3K27me3 in mediating gene repression to control neuronal maturation timing, similar to the role defined here for DNMT3A during GABAergic neuron development. Relevant to these overlapping mechanisms of gene repression controling neuronal maturation, pathogenic *EZH2* mutation causes Weaver Syndrome, another OGID[31-33]. While relatively understudied, limited mouse studies associated *EZH2* mutation with bone overgrowth[77], while EZH2 LOF mouse models exhibited deficits in neuronal differentiation and maturation[78]. These and our findings support interconnected requirements for DNMT3A and EZH2 in neuronal gene regulation, with disruption of either contributing to OGID etiology. Likewise, another associated OGID (Sotos Syndrome) involves mutations in the histone methyltransferase *NSD1*[79-81], which influences DNMT3A-mediated DNA methylation[82,83]. These human TBRS models and data provide a foundation for future work to define convergent cellular phenotypes across related OGID syndromes. Together, this work highlights GABAergic neurons as highly sensitive to TBRS-associated DNMT3A LOF and defines key molecular and functional alterations; these can both be used to probe phenotypic convergence across OGID syndromes and provide a platform for future studies to identify interventions that can normalize neuronal network anomalies underlying TBRS and other OGID syndromes.

Data availability

The data used and generated in this study are provided in the Supplementary material where appropriate with raw data available from GEO under accession numbers GSE294189, GSE294191 and GSE294186 or dbgap under accession number XXX.

Acknowledgements

We thank the Genome Technology Access Center at the McDonnell Genome Institute (GTAC@MGI) at Washington University School of Medicine for help with genomics services. We also thank the Genome Engineering & Stem Cell Center (GESC@MGI) at Washington University in St. Louis for cell line engineering services. Finally, we thank the Ley lab for their work in developing and characterizing the DNMT3A R882H iPSC line used in this study, and in particular Daniel George and Dr. Christopher A. Miller.

Funding

This work was supported by NIH Grants R01NS114551, R01MH124808, R01HD110556, and U0-HG007530 (NIH Common Fund/NINDS Undiagnosed Disease Network pilot gene study subaward) to KLK, and by NIH P50HD103525 to Joseph Dougherty and Christina Gurnett (KLK is project PI for the Human Cellular Models Unit of the Washington University Intellectual and Developmental Disabilities Research Center, with project effort funded by this grant). Foundations supporting this work included the Engelhart Family Foundation, Simons Foundation, M-CM Network, and pilot awards from the WU Hope Center, Center of Regenerative Medicine, and Institute for Clinical and Translational Sciences to KLK. GTAC@MGI is partially supported by NCI Cancer Center Support Grant #P30 CA91842 to the Siteman Cancer Center from the National Center for Research Resources (NCRR), a component of the National Institutes of Health (NIH), and NIH Roadmap for Medical Research. Work conducted in the Ley laboratory was supported by NIH CA197161.

Competing Interests

The authors declare no competing interests

References

1 Libe-Philippot, B. & Vanderhaeghen, P. Cellular and Molecular Mechanisms Linking Human Cortical Development and Evolution. *Annu Rev Genet* **55**, 555-581 (2021). https://doi.org/10.1146/annurev-genet-071719-020705

2 Toma, K., Wang, T. C. & Hanashima, C. Encoding and decoding time in neural development. *Dev Growth Differ* **58**, 59-72 (2016). https://doi.org/10.1111/dgd.12257

3 Zhu, Y. *et al.* Spatiotemporal transcriptomic divergence across human and macaque brain development. *Science* **362** (2018). https://doi.org/10.1126/science.aat8077

4 Marchetto, M. C. *et al.* Species-specific maturation profiles of human, chimpanzee and bonobo neural cells. *Elife* **8** (2019). https://doi.org/10.7554/eLife.37527

5 Chapman, G. *et al.* Defining cis-regulatory elements and transcription factors that control human cortical interneuron development. *iScience* **27**, 109967 (2024). https://doi.org/10.1016/j.isci.2024.109967

6 Lim, L., Mi, D., Llorca, A. & Marin, O. Development and Functional Diversification of Cortical Interneurons. *Neuron* **100**, 294-313 (2018). https://doi.org/10.1016/j.neuron.2018.10.009

7 Zecevic, N., Hu, F. & Jakovcevski, I. Interneurons in the developing human neocortex. *Dev Neurobiol* **71**, 18-33 (2011). https://doi.org/10.1002/dneu.20812

8 Le Magueresse, C. & Monyer, H. GABAergic interneurons shape the functional maturation of the cortex. *Neuron* **77**, 388-405 (2013). https://doi.org/10.1016/j.neuron.2013.01.011

9 Warm, D., Schroer, J. & Sinning, A. Gabaergic Interneurons in Early Brain Development: Conducting and Orchestrated by Cortical Network Activity. *Front Mol Neurosci* **14**, 807969 (2021). https://doi.org/10.3389/fnmol.2021.807969

10 Heesen, S. H. & Kohr, G. GABAergic interneuron diversity and organization are crucial for the generation of human-specific functional neural networks in cerebral organoids. *Front Cell Neurosci* **18**, 1389335 (2024). https://doi.org/10.3389/fncel.2024.1389335

11 Arzate-Mejia, R. G. & Mansuy, I. M. Remembering through the genome: the role of chromatin states in brain functions and diseases. *Transl Psychiatry* **13**, 122 (2023). https://doi.org/10.1038/s41398-023-02415-4

12 Lossi, L., Castagna, C. & Merighi, A. An Overview of the Epigenetic Modifications in the Brain under Normal and Pathological Conditions. *Int J Mol Sci* **25** (2024). https://doi.org/10.3390/ijms25073881

13 MacDonald, J. L. & Roskams, A. J. Epigenetic regulation of nervous system development by DNA methylation and histone deacetylation. *Prog Neurobiol* **88**, 170-183 (2009). https://doi.org/10.1016/j.pneurobio.2009.04.002

14 Tatton-Brown, K. *et al.* Mutations in Epigenetic Regulation Genes Are a Major Cause of Overgrowth with Intellectual Disability. *Am J Hum Genet* **100**, 725-736 (2017). https://doi.org/10.1016/j.ajhg.2017.03.010

15 Lane, C., Tatton-Brown, K. & Freeth, M. Tatton-Brown-Rahman syndrome: cognitive and behavioural phenotypes. *Dev Med Child Neurol* **62**, 993-998 (2020). https://doi.org/10.1111/dmcn.14426

16 Ostrowski, P. J. & Tatton-Brown, K. in *GeneReviews((R))* (eds M. P. Adam *et al.*) (1993).

17 Tatton-Brown, K. *et al.* The Tatton-Brown-Rahman Syndrome: A clinical study of 55 individuals with de novo constitutive DNMT3A variants. *Wellcome Open Res* **3**, 46 (2018). https://doi.org/10.12688/wellcomeopenres.14430.1

18 Thomas, H. *et al.* Expanding the genetic and clinical spectrum of Tatton-Brown-Rahman syndrome in a series of 24 French patients. *J Med Genet* (2024). https://doi.org/10.1136/jmg-2024-110031
19 Smith, A. M. *et al.* Functional and epigenetic phenotypes of humans and mice with DNMT3A Overgrowth Syndrome. *Nat Commun* **12**, 4549 (2021). https://doi.org/10.1038/s41467-021-24800-7
20 Tenorio, J. *et al.* Further delineation of neuropsychiatric findings in Tatton-Brown-Rahman syndrome due to disease-causing variants in DNMT3A: seven new patients. *Eur J Hum Genet* **28**, 469-479 (2020). https://doi.org/10.1038/s41431-019-0485-3
21 Christian, D. L. *et al.* DNMT3A Haploinsufficiency Results in Behavioral Deficits and Global Epigenomic Dysregulation Shared across Neurodevelopmental Disorders. *Cell Rep* **33**, 108416 (2020). https://doi.org/10.1016/j.celrep.2020.108416
22 Sanson, K. R. *et al.* Optimized libraries for CRISPR-Cas9 genetic screens with multiple modalities. *Nat Commun* **9**, 5416 (2018). https://doi.org/10.1038/s41467-018-07901-8
23 Chapman, G. *et al.* Using induced pluripotent stem cells to investigate human neuronal phenotypes in 1q21.1 deletion and duplication syndrome. *Mol Psychiatry* **27**, 819-830 (2022). https://doi.org/10.1038/s41380-021-01182-2
24 Schafer, S. T. *et al.* Pathological priming causes developmental gene network heterochronicity in autistic subject-derived neurons. *Nat Neurosci* **22**, 243-255 (2019). https://doi.org/10.1038/s41593-018-0295-x
25 Stirling, D. R. *et al.* CellProfiler 4: improvements in speed, utility and usability. *BMC Bioinformatics* **22**, 433 (2021). https://doi.org/10.1186/s12859-021-04344-9
26 Ross-Innes, C. S. *et al.* Differential oestrogen receptor binding is associated with clinical outcome in breast cancer. *Nature* **481**, 389-393 (2012). https://doi.org/10.1038/nature10730
27 Meganathan, K. *et al.* Regulatory networks specifying cortical interneurons from human embryonic stem cells reveal roles for CHD2 in interneuron development. *Proc Natl Acad Sci U S A* **114**, E11180-E11189 (2017). https://doi.org/10.1073/pnas.1712365115
28 Nguyen, T. V. *et al.* The R882H DNMT3A hot spot mutation stabilizes the formation of large DNMT3A oligomers with low DNA methyltransferase activity. *J Biol Chem* **294**, 16966-16977 (2019). https://doi.org/10.1074/jbc.RA119.010126
29 Lewis, E. M. A. *et al.* Regulation of human cortical interneuron development by the chromatin remodeling protein CHD2. *Sci Rep* **12**, 15636 (2022). https://doi.org/10.1038/s41598-022-19654-y
30 Ciceri, G. *et al.* An epigenetic barrier sets the timing of human neuronal maturation. *Nature* **626**, 881-890 (2024). https://doi.org/10.1038/s41586-023-06984-8
31 Gibson, W. T. *et al.* Mutations in EZH2 cause Weaver syndrome. *Am J Hum Genet* **90**, 110-118 (2012). https://doi.org/10.1016/j.ajhg.2011.11.018
32 Tatton-Brown, K. *et al.* Weaver syndrome and EZH2 mutations: Clarifying the clinical phenotype. *Am J Med Genet A* **161A**, 2972-2980 (2013). https://doi.org/10.1002/ajmg.a.36229
33 Cohen, A. S. *et al.* Weaver Syndrome-Associated EZH2 Protein Variants Show Impaired Histone Methyltransferase Function In Vitro. *Hum Mutat* **37**, 301-307 (2016). https://doi.org/10.1002/humu.22946
34 Beard, D. C. *et al.* Distinct disease mutations in DNMT3A result in a spectrum of behavioral, epigenetic, and transcriptional deficits. *Cell Rep* **42**, 113411 (2023). https://doi.org/10.1016/j.celrep.2023.113411

35 Wang, M. *et al.* Increased Neural Progenitor Proliferation in a hiPSC Model of Autism Induces Replication Stress-Associated Genome Instability. *Cell Stem Cell* **26**, 221-233 e226 (2020). https://doi.org/10.1016/j.stem.2019.12.013
36 Connacher, R. *et al.* Autism NPCs from both idiopathic and CNV 16p11.2 deletion patients exhibit dysregulation of proliferation and mitogenic responses. *Stem Cell Reports* **17**, 1786 (2022). https://doi.org/10.1016/j.stemcr.2022.06.007
37 Marchetto, M. C. *et al.* Altered proliferation and networks in neural cells derived from idiopathic autistic individuals. *Mol Psychiatry* **22**, 820-835 (2017). https://doi.org/10.1038/mp.2016.95
38 Ernst, C. Proliferation and Differentiation Deficits are a Major Convergence Point for Neurodevelopmental Disorders. *Trends Neurosci* **39**, 290-299 (2016). https://doi.org/10.1016/j.tins.2016.03.001
39 Packer, A. Neocortical neurogenesis and the etiology of autism spectrum disorder. *Neurosci Biobehav Rev* **64**, 185-195 (2016). https://doi.org/10.1016/j.neubiorev.2016.03.002
40 Aldridge, A. I. & West, A. E. Epigenetics and the timing of neuronal differentiation. *Curr Opin Neurobiol* **89**, 102915 (2024). https://doi.org/10.1016/j.conb.2024.102915
41 Coskun, V., Tsoa, R. & Sun, Y. E. Epigenetic regulation of stem cells differentiating along the neural lineage. *Curr Opin Neurobiol* **22**, 762-767 (2012). https://doi.org/10.1016/j.conb.2012.07.001
42 Markicevic, M. *et al.* Cortical Excitation:Inhibition Imbalance Causes Abnormal Brain Network Dynamics as Observed in Neurodevelopmental Disorders. *Cereb Cortex* **30**, 4922-4937 (2020). https://doi.org/10.1093/cercor/bhaa084
43 Gatto, C. L. & Broadie, K. Genetic controls balancing excitatory and inhibitory synaptogenesis in neurodevelopmental disorder models. *Front Synaptic Neurosci* **2**, 4 (2010). https://doi.org/10.3389/fnsyn.2010.00004
44 Pietropaolo, S. & Provenzano, G. Editorial: Targeting Excitation-Inhibition Imbalance in Neurodevelopmental and Autism Spectrum Disorders. *Front Neurosci* **16**, 968115 (2022). https://doi.org/10.3389/fnins.2022.968115
45 Canitano, R. & Pallagrosi, M. Autism Spectrum Disorders and Schizophrenia Spectrum Disorders: Excitation/Inhibition Imbalance and Developmental Trajectories. *Front Psychiatry* **8**, 69 (2017). https://doi.org/10.3389/fpsyt.2017.00069
46 Uzunova, G., Pallanti, S. & Hollander, E. Excitatory/inhibitory imbalance in autism spectrum disorders: Implications for interventions and therapeutics. *World J Biol Psychiatry* **17**, 174-186 (2016). https://doi.org/10.3109/15622975.2015.1085597
47 Lunden, J. W., Durens, M., Phillips, A. W. & Nestor, M. W. Cortical interneuron function in autism spectrum condition. *Pediatr Res* **85**, 146-154 (2019). https://doi.org/10.1038/s41390-018-0214-6
48 Tang, X., Jaenisch, R. & Sur, M. The role of GABAergic signalling in neurodevelopmental disorders. *Nat Rev Neurosci* **22**, 290-307 (2021). https://doi.org/10.1038/s41583-021-00443-x
49 Filice, F., Schwaller, B., Michel, T. M. & Grunblatt, E. Profiling parvalbumin interneurons using iPSC: challenges and perspectives for Autism Spectrum Disorder (ASD). *Mol Autism* **11**, 10 (2020). https://doi.org/10.1186/s13229-020-0314-0
50 Wang, P., Zhao, D., Lachman, H. M. & Zheng, D. Enriched expression of genes associated with autism spectrum disorders in human inhibitory neurons. *Transl Psychiatry* **8**, 13 (2018). https://doi.org/10.1038/s41398-017-0058-6
51 Culotta, L. & Penzes, P. Exploring the mechanisms underlying excitation/inhibition imbalance in human iPSC-derived models of ASD. *Mol Autism* **11**, 32 (2020). https://doi.org/10.1186/s13229-020-00339-0

52 Mariani, J. *et al.* FOXG1-Dependent Dysregulation of GABA/Glutamate Neuron Differentiation in Autism Spectrum Disorders. *Cell* **162**, 375-390 (2015). https://doi.org/10.1016/j.cell.2015.06.034
53 Xu, L. *et al.* Abnormal mitochondria in Down syndrome iPSC-derived GABAergic interneurons and organoids. *Biochim Biophys Acta Mol Basis Dis* **1868**, 166388 (2022). https://doi.org/10.1016/j.bbadis.2022.166388
54 Ni, P. *et al.* Correction: iPSC-derived homogeneous populations of developing schizophrenia cortical interneurons have compromised mitochondrial function. *Mol Psychiatry* **25**, 3103-3104 (2020). https://doi.org/10.1038/s41380-019-0467-4
55 Kathuria, A. *et al.* Synaptic deficits in iPSC-derived cortical interneurons in schizophrenia are mediated by NLGN2 and rescued by N-acetylcysteine. *Transl Psychiatry* **9**, 321 (2019). https://doi.org/10.1038/s41398-019-0660-x
56 Kadriu, B., Guidotti, A., Chen, Y. & Grayson, D. R. DNA methyltransferases1 (DNMT1) and 3a (DNMT3a) colocalize with GAD67-positive neurons in the GAD67-GFP mouse brain. *J Comp Neurol* **520**, 1951-1964 (2012). https://doi.org/10.1002/cne.23020
57 Tomassy, G. S., Morello, N., Calcagno, E. & Giustetto, M. Developmental abnormalities of cortical interneurons precede symptoms onset in a mouse model of Rett syndrome. *J Neurochem* **131**, 115-127 (2014). https://doi.org/10.1111/jnc.12803
58 Gabel, H. W. *et al.* Disruption of DNA-methylation-dependent long gene repression in Rett syndrome. *Nature* **522**, 89-93 (2015). https://doi.org/10.1038/nature14319
59 Clemens, A. W. *et al.* MeCP2 Represses Enhancers through Chromosome Topology-Associated DNA Methylation. *Mol Cell* **77**, 279-293 e278 (2020). https://doi.org/10.1016/j.molcel.2019.10.033
60 Sandweiss, A. J., Brandt, V. L. & Zoghbi, H. Y. Advances in understanding of Rett syndrome and MECP2 duplication syndrome: prospects for future therapies. *Lancet Neurol* **19**, 689-698 (2020). https://doi.org/10.1016/S1474-4422(20)30217-9
61 Lu, H. *et al.* Loss and Gain of MeCP2 Cause Similar Hippocampal Circuit Dysfunction that Is Rescued by Deep Brain Stimulation in a Rett Syndrome Mouse Model. *Neuron* **91**, 739-747 (2016). https://doi.org/10.1016/j.neuron.2016.07.018
62 Guy, J., Cheval, H., Selfridge, J. & Bird, A. The role of MeCP2 in the brain. *Annu Rev Cell Dev Biol* **27**, 631-652 (2011). https://doi.org/10.1146/annurev-cellbio-092910-154121
63 Pantier, R. *et al.* MeCP2 binds to methylated DNA independently of phase separation and heterochromatin organisation. *Nat Commun* **15**, 3880 (2024). https://doi.org/10.1038/s41467-024-47395-1
64 Landucci, E. *et al.* iPSC-derived neurons profiling reveals GABAergic circuit disruption and acetylated alpha-tubulin defect which improves after iHDAC6 treatment in Rett syndrome. *Exp Cell Res* **368**, 225-235 (2018). https://doi.org/10.1016/j.yexcr.2018.05.001
65 Ure, K. *et al.* Restoration of Mecp2 expression in GABAergic neurons is sufficient to rescue multiple disease features in a mouse model of Rett syndrome. *Elife* **5** (2016). https://doi.org/10.7554/eLife.14198
66 Mok, R. S. F. *et al.* Wide spectrum of neuronal and network phenotypes in human stem cell-derived excitatory neurons with Rett syndrome-associated MECP2 mutations. *Transl Psychiatry* **12**, 450 (2022). https://doi.org/10.1038/s41398-022-02216-1
67 Alsaqati, M., Heine, V. M. & Harwood, A. J. Pharmacological intervention to restore connectivity deficits of neuronal networks derived from ASD patient iPSC with a TSC2 mutation. *Mol Autism* **11**, 80 (2020). https://doi.org/10.1186/s13229-020-00391-w

68 Rylaarsdam, L., Rakotomamonjy, J., Pope, E. & Guemez-Gamboa, A. iPSC-derived models of PACS1 syndrome reveal transcriptional and functional deficits in neuron activity. *Nat Commun* **15**, 827 (2024). https://doi.org/10.1038/s41467-024-44989-7
69 Deneault, E. *et al.* CNTN5(-)(/+)or EHMT2(-)(/+)human iPSC-derived neurons from individuals with autism develop hyperactive neuronal networks. *Elife* **8** (2019). https://doi.org/10.7554/eLife.40092
70 Deneault, E. *et al.* Complete Disruption of Autism-Susceptibility Genes by Gene Editing Predominantly Reduces Functional Connectivity of Isogenic Human Neurons. *Stem Cell Reports* **12**, 427-429 (2019). https://doi.org/10.1016/j.stemcr.2019.01.008
71 DeRosa, B. A. *et al.* Author Correction: Convergent Pathways in Idiopathic Autism Revealed by Time Course Transcriptomic Analysis of Patient-Derived Neurons. *Sci Rep* **12**, 3445 (2022). https://doi.org/10.1038/s41598-022-07356-4
72 Amatya, D. N. *et al.* Dynamical Electrical Complexity Is Reduced during Neuronal Differentiation in Autism Spectrum Disorder. *Stem Cell Reports* **13**, 474-484 (2019). https://doi.org/10.1016/j.stemcr.2019.08.001
73 Graef, J. D. *et al.* Partial FMRP expression is sufficient to normalize neuronal hyperactivity in Fragile X neurons. *Eur J Neurosci* **51**, 2143-2157 (2020). https://doi.org/10.1111/ejn.14660
74 Nageshappa, S. *et al.* Altered neuronal network and rescue in a human MECP2 duplication model. *Mol Psychiatry* **21**, 178-188 (2016). https://doi.org/10.1038/mp.2015.128
75 Frega, M. *et al.* Neuronal network dysfunction in a model for Kleefstra syndrome mediated by enhanced NMDAR signaling. *Nat Commun* **10**, 4928 (2019). https://doi.org/10.1038/s41467-019-12947-3
76 Li, J. *et al.* Dnmt3a knockout in excitatory neurons impairs postnatal synapse maturation and increases the repressive histone modification H3K27me3. *Elife* **11** (2022). https://doi.org/10.7554/eLife.66909
77 Gao, C. W. *et al.* A mouse model of Weaver syndrome displays overgrowth and excess osteogenesis reversible with KDM6A/6B inhibition. *JCI Insight* **9** (2024). https://doi.org/10.1172/jci.insight.173392
78 Pereira, J. D. *et al.* Ezh2, the histone methyltransferase of PRC2, regulates the balance between self-renewal and differentiation in the cerebral cortex. *Proc Natl Acad Sci U S A* **107**, 15957-15962 (2010). https://doi.org/10.1073/pnas.1002530107
79 Hamagami, N. *et al.* NSD1 deposits histone H3 lysine 36 dimethylation to pattern non-CG DNA methylation in neurons. *Molecular Cell* **83**, 1412-1428.e1417 (2023). https://doi.org/https://doi.org/10.1016/j.molcel.2023.04.001
80 Brennan, K. *et al.* NSD1 mutations deregulate transcription and DNA methylation of bivalent developmental genes in Sotos syndrome. *Hum Mol Genet* **31**, 2164-2184 (2022). https://doi.org/10.1093/hmg/ddac026
81 Choufani, S. *et al.* NSD1 mutations generate a genome-wide DNA methylation signature. *Nat Commun* **6**, 10207 (2015). https://doi.org/10.1038/ncomms10207
82 Tatton-Brown, K. & Rahman, N. Sotos syndrome. *Eur J Hum Genet* **15**, 264-271 (2007). https://doi.org/10.1038/sj.ejhg.5201686
83 Leventopoulos, G. *et al.* A clinical study of Sotos syndrome patients with review of the literature. *Pediatr Neurol* **40**, 357-364 (2009). https://doi.org/10.1016/j.pediatrneurol.2008.11.013

Figure Legends

Figure 1. TBRS-associated *DNMT3A* mutations cause increased proliferation and precocious neuronal gene expression.

a, R882H hPSC model was generated by reprogramming peripheral blood mononuclear cells (PBMCs) from a subject with the mutation, with CRISPR-Cas9-based correction to generate the isogenic control. **b,** P904L hPSC model was generated by heterozygous variant knock-in to wildtype hPSCs, which serve as an isogenic control. Neural progenitors with **c**, dorsal telencephalic (D-NPC) or **d,** ventral telencephalic (V-NPC) character were specified from hPSCs by day (D)20 and D15, respectively. **e**, Representative images indicate plated V-NPC sphere size (solid lines) and extent of outgrowth (dotted lines), with relative outgrowth quantified and normalized to sphere size at D12. **f**, Representative images and quantification of the Ki-67 immunopositive V-NPC fraction. **g**, Top representative gene ontology (GO) terms and **h**, differential expression of DEGs with significantly increased expression in both TBRS V-NPCs versus their isogenic controls. **i**, Lentiviral CRISPRi knockdown (KD) targets dCas9-KRAB to the DNMT3A promotor using G1 or G2 gRNA, with controls expressing dCas9-KRAB without gRNA. **j-k**, Quantification of DNMT3A (**j**) mRNA and (**k**) protein in control versus CRISPRi models. **l,** Representative images of sphere size (solid lines) and outgrowth (dotted lines), and quantification for control (KRAB) or KD D12 V-NPC spheres. **m**, Representative images and quantification of Ki-67 immunopositive fraction of control (KRAB) and KD V-NPCs (D12). **n**, RT-qPCR confirmed dose-dependent differential expression of TBRS-shared DEGs in TBRS and KD models, with related GO terms indicated. Data is represented as mean +/- SEM (**f,j,k,m,n**) with individual biological replicates indicated (**f,j,k,m**) or as distributions with median (bold line) and upper and lower quartiles (dotted lines) indicated (**e,l**) and was analyzed by Students T-Test, versus isogenic controls (**e,f,j,k,l,m,n**). n=4 biological replicate experiments for all conditions, pValues: *p<0.05;**p<0.01;***p<0.001;****p<0.0001. Scale bars=50 µm (**e,f,l,m**).

Fig 2. DNA methylation regulated by DNMT3A controls neuronal gene expression onset in V-NPCs.

a, mCG/CG levels in control (C-WT) versus 882 V-NPCs. **b**, Heat map of relative mCG levels at 882 V-NPC DMRs. **c**, Overlap of 882 V-NPC DMRs with key DNA methylation-related genomic regions, indicating hypo-/hyper-DMRs alongside averaged resampled hypo-/hyper-DMRs. **d**, Gene expression changes at genes associated with 882 V-NPC hypoDMRs. Genes

up- (left) versus down-regulated (right) in 882 V-NPCs were segregated and data compared to all genes associated with 882 V-NPC hypoDMRs (segregated by directionality for statistical analysis). **e**, Representative results from GO analysis of genes associated with 882 V-NPC hypo-DMRs and with significantly increased expression in 882 V-NPCs versus isogenic control V-NPCs (882 DEGs). **f**, Genomic browser views of mCG in C-WT and 882 V-NPCs, highlighting (red) hypo-DMRs associated with promotors of upregulated 882 versus control DEGs in V-NPCs (GRIP2-Top, SYT3-Middle and SHANK1-bottom). **g**, mCG/CG differences at 882 and 904 DMRs, qualified by DMR type (hyper/hypo) in both (882 and 904) or specifically 882 V-NPCs. **h**, Representative top GO terms for genes associated with an 882 and 904 V-NPC hypo-DMR with significantly increased expression in 882 and 904 V-NPCs versus isogenic control V-NPCs. Data is represented as mean+/-SEM (**a**,**d**,**f**,**g**) with individual biological replicates indicated (**a**,**b**,**g**). Data was analyzed by Students T-Test versus isogenic controls (**a**,**d**), by Fisher's exact test comparing observed versus background estimated from 100X-resampled DMRs (**c**) or by differential expression analysis (**e**). n=4 biological replicate experiments for all conditions, pValues: *p<0.05;**p<0.01;***p<0.001;****p<0.0001;n.s.-non-significant.

Fig 3. Increased H3K27me3 specifically compensates for loss of DNA methylation in R882H NPCs.

a, H3K27me3 signal across 5kb region centered on 882 hypo-DMRs in control (WT) hPSCs, V-NPCs and V-INs. **b**, H3K27me3 peaks with significantly increased (hyper-DKS) or decreased (hypo-DKS) enrichment in 882 versus control V-NPCs. **c**, Quantification of percentages of DKSs overlapping 882 hypo- or hyper-DMRs. **d**, Representative results from GO analysis of genes associated with hypo-DMRs and hypo-DKSs in 882 V-NPCs. **e**, H3K27me3 peaks with significantly increased (hyper-DKS) or decreased (hypo-DKS) enrichment in 882 versus control D-NPCs. **f**, Expression of genes associated with hypo-DMRs and hypo-DKSs in 882 NPCs (D and V) across both hPSC-dorsal and hPSC-ventral differentiation. **g**, Representative results from GO analysis of non-DEGs associated with hypo-DMRs and hypo-DKSs in 882 NPCs (D and V). **h**, Genomic browser views of mCG and H3K27me3 in 882 and control V-NPCs, highlighting (red) hypo-DMRs and hyper-DKSs associated with promotors of two genes (ESRG-left; ARX-right). **i**, Experimental paradigm for assessing how EZH2 inhibition (EZH2i) of H3K27me3 in D-NPCs carrying TBRS-associated mutations affects gene expression. **j**, RT-qPCR was used to assess the effect of EZH2i on

expression of key genes identified as non-responsive to DNMT3A LOF in 882, due to compensatory H3K27me3 increase. Data represented as mean+/-SEM. (**j**). Data was analyzed by Students T-Test, versus isogenic controls (**j**) or by differential binding analysis (**b**,**e**). n=4 biological replicate experiments for all conditions, (**j**) *pValue<0.05.

Fig 4. DNMT3A constrains the expression of synaptic genes in V-INs.

a, Experimental paradigm for generating immature GABAergic neurons (V-INs) from ventrally patterned neuronal progenitors (V-NPCs). **b,** Principal component analysis of control (grey) and TBRS V-INs (882-blue and 904-orange). **c,** Representative results from gene ontology (GO) analysis of genes up regulated in 882 V-INs versus C-WT V-INs. **d,** Representative results from GO analysis of genes up regulated in TBRS V-INs as compared to control V-INs. **e,** Heatmap of genes associated with the 'synapse' GO term up regulated in TBRS V-INs. **f,** Changes in global mCG/CG levels in DNA isolated from C-WT and 882 V-INs. **g,** Changes in mCG/CG at 882, 904, or TBRS V-IN hypo-DMRs in both TBRS and control V-INs. **h,** Genomic browser views of mCG in TBRS and control V-INs, highlighting (red) a TBRS-shared hypo-DMR associated with the promotor of the 'synapse' associated gene KCNN3. **i**, Changes in mCG/CG at TBRS-shared hypo-DMRs identified in V-NPCs or V-INs across both TBRS and control V-NPCs and V-INs. Data was analyzed by Students T-Test versus isogenically matched controls (**f,g,i**), n=4 biological replicate experiments for all conditions, (**f,g,i**) ***pValue<0.001, ****pValue<0.0001.

Fig 5. Loss of DNMT3A function during D-IN differentiation results in increased expression of early neurodevelopmental gene expression programs.

a, Experimental paradigm for generating immature cortical glutamatergic neurons (D-INs) from dorsally patterned neuronal progenitors (D-NPCs). **b**, Principal component analysis of transcriptomic data from control (grey) and TBRS D-INs (882-blue and 904-orange). **c**, Heatmap representing change in expression of all DEGs up-regulated in 882 and 904 D-INs versus their isogenic controls, across all D-IN samples. **d**, Representative results from GO analysis of genes with significantly increased expression in both 882 and 904 D-INs versus isogenic control D-INs. **e**, Change in expression across hPSC-D-IN differentiation of all DEGs up-regulated in 882 and 904 V-INs versus isogenic controls. **f,** Experimental paradigm for generating cortical glutamatergic-like neurons (iGluts), by direct reprogramming with

inducible Neurogenin2 (NGN2) overexpression. **g**, Principal component analysis of control (grey) and TBRS iGluts (882-blue, 904-orange). **h**, Representative results from GO analysis of genes up-regulated in either 882 or 904 iGluts versus isogenic iGlut controls. **i**, Genome browser views of mCG in control (grey) and 904 (orange) iGluts, highlighting the occurrence of both hypo- (blue) and hyper-DMRs (red) near the *NOTCH1* and *TGFB1* transcription start sites. **j**, mCG/CG levels at TBRS-shared hypo-DMRs identified in D-INs or iGluts, across both TBRS and control D-INs or iGluts. **k**, mCG/CG levels at TBRS-shared hypo-DMRs identified in D-INs or V-INs across both TBRS and control D-INs or V-INs. **l**, Genomic locations of TBRS-shared hypo-DMRs identified in both D- and V-INs. **m**, Representative results from GO analysis of genes associated with TBRS-shared hypo-DMRs in both D- and V-INs. Data was analyzed by two-way ANOVA, with posthoc Tukey's multiple comparison testing, comparing TBRS and control samples in (**j**,**k**); n=4 biological replicate experiments for all D- and V-IN conditions in (**b**,**c**,**d**,**e**,**j**,**k**,**m**); n=3 biological replicate experiments for all iGlut conditions in (**g**,**h**,**j**); *pValue<0.05;****pValue<0.0005.

Fig 6. TBRS-associated mutations in *DNMT3A* cause GABAergic neuron hyperactivity.

a-h, Patch-clamp electrophysiology in day 60 V-INs, comparing 882 (blue) and control (grey) neurons. **a,** Resting membrane potential (mV) demonstrated no significant difference across the cell membrane under neutral conditions, indicating cells are equally healthy. **b,** Example of electrophysiological traces at 120pA current over 1 second, highlighting higher and more narrow action potentials in the 882 GABAergic neurons. **c,** Maximum numbers of spikes (count), demonstrating that 882 GABAergic neurons fire more frequently, **d,** action potential (AP) halfwidth (ms), showing that 882 GABAergic neuron peaks are narrower, and (**e)** action potential (AP) height (mV), showing that 882 GABAergic neuron peaks are higher than control. **f,** sodium (Na) current density at 0 mV, normalized by capacitance (pA/pf), demonstrating 882 GABAergic neurons have a higher response when stimulated by voltage step, and (**g**) transient outward current, normalized by capacitance (pA/pf), demonstrating that 882 GABAergic neurons have more potassium current across the cell membrane after a voltage step. **h,** Inward sodium current and transient outward potassium current during voltage step from -80 to -10 mV, highlighting increases in 882 GABAergic neurons. **i-j,** Patch-clamp electrophysiology of WT (grey) and 904 (orange) neurons, with (**i**) day 60 V-IN electrophysiological traces at 120pA over 1 second and (**j**) maximum number of spikes (count)

measured in both V-IN and D-IN neurons, highlighting an overall effect of 904 mutation on neuronal activity. Significance was calculated by Rank Sum Test and results are presented as mean+/-SEM, *pValue<0.05;**pValue<0.01;***pValue<0.001.

Fig 7. Abnormal neuronal network development associated with TBRS models is driven by GABAergic neuron dysfunction.

(a-d), 70/30 co-cultures of D-IN/V-IN neurons, both of which were either 882 or control (C-WT) genotype, were measured by low-density multielectrode array (LD-MEA) from D55-D80. **a,** Representative raster plots of activity from early (D55, left) to late (D80, right) time points, with synchronized activity indicated by red boxes. **b,** Changes in mean firing rate across time, highlighting increased mean firing rate in 882 model ($F_{1,6}$=6.579, pValue<0.05, n=4). **c,** Changes in number of network bursts in 10-minute recording, highlighting significant increase in 882 model ($F_{1,6}$=12.18, pValue<0.05, n=4). **d,** Changes in network burst duration. (**e-o)** Control iGluts were co-cultured at 70/30 ratio with either TBRS (882-blue; 904-orange) or isogenic control (gray) GABAergic neurons and assessed by high density multielectrode arrays (HD-MEA). In e-g HD-MEA recordings were performed at D50 of GABAergic neuron differentiation and include: **e,** representative raster plots of activity, with bursting highlighted by horizontal lines for each electrode, **f,** mean firing rate, and **g,** numbers of bursting electrodes (defined as an electrode with >2 bursts per 10-minute recording), as defined in 70/30 co-cultures of control iGluts with TBRS or control GABAergic neurons. In **h-o,** HD-MEA recordings were performed at D82 of GABAergic neuron differentiation and include: **h,** Representative raster plots of neuronal activity, with electrode bursting activity highlighted by horizontal lines for each electrode, **i,** Changes in mean firing rate, **j,** Quantification of the number of spikes per burst, **k,** Quantification of the mean inter-spike-interval (ISI) for spikes within electrode bursts, **l,** Changes in the neuronal network bursting frequency, **m,** Quantifications of network burst duration, **n,** Quantification of the percentage of spikes (activity) found in network bursts, and **o,** Quantification of the mean inter-spike-interval (ISI) of spikes within network bursts, with all work performed in cultures of control iGluts and control (C-WT, WT) or TBRS (882 or 904) GABAergic neurons at D82 of GABAergic neuron differentiation. Data was analyzed by two-way ANOVA, with posthoc Tukey's multiple comparison testing comparing TBRS and control samples (**b-d**), or via Student's T-Test (**f,g,i,j,k,l,n**) or Mann-Whitney test (**m,o**), versus isogenic controls; n=4 biological replicate

experiments for all experiments (**b-d**,**f**,**g**,**i-o**), *pValue<0.05;**pValue<0.01;***pValue<0.001; ****pValue<0.0001;n.s.=not significant,.

Fig. 1

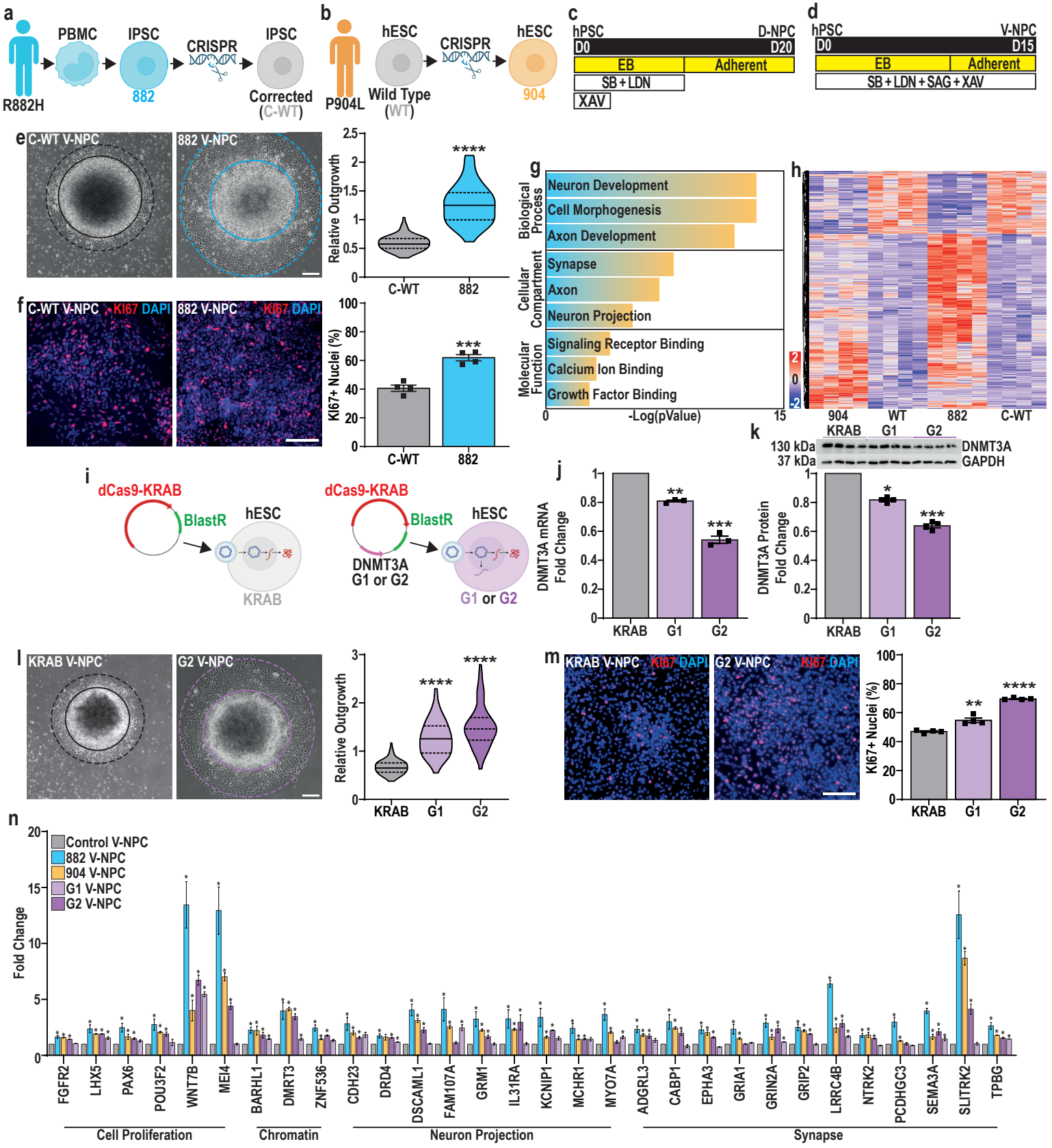
a
PBMC
IPSC
CRISPR
IPSC
R882H
882
Corrected
(C-WT)
b
hESC
CRISPR
hESC
P904L
Wild Type
(WT)
904
c
hPSC
D-NPC
D0
D20
EB
Adherent
SB + LDN
XAV
d
hPSC
V-NPC
D0
D15
EB
Adherent
SB + LDN + SAG + XAV
e
C-WT V-NPC
882 V-NPC
Relative Outgrowth
****
C-WT
882
f
C-WT V-NPC
KI67 DAPI
882 V-NPC
KI67 DAPI
KI67+ Nuclei (%)
***
C-WT
882
g
Biological Process
Neuron Development
Cell Morphogenesis
Axon Development
Cellular Compartment
Synapse
Axon
Neuron Projection
Molecular Function
Signaling Receptor Binding
Calcium Ion Binding
Growth Factor Binding
-Log(pValue)
h
904
WT
882
C-WT
i
dCas9-KRAB
BlastR
hESC
KRAB
dCas9-KRAB
BlastR
hESC
DNMT3A
G1 or G2
G1 or G2
j
DNMT3A mRNA Fold Change
KRAB
G1
G2
k
KRAB
G1
G2
130 kDa
DNMT3A
37 kDa
GAPDH
DNMT3A Protein Fold Change
l
KRAB V-NPC
G2 V-NPC
Relative Outgrowth
****
****
KRAB
G1
G2
m
KRAB V-NPC
KI67 DAPI
G2 V-NPC
KI67 DAPI
KI67+ Nuclei (%)
**
****
KRAB
G1
G2
n
Control V-NPC
882 V-NPC
904 V-NPC
G1 V-NPC
G2 V-NPC
Fold Change
FGFR2
LHX5
PAX6
POU3F2
WNT7B
MEI4
BARHL1
DMRT3
ZNF536
CDH23
DRD4
DSCAML1
FAM107A
GRM1
IL31RA
KCNIP1
MCHR1
MYO7A
ADGRL3
CABP1
EPHA3
GRIA1
GRIN2A
GRIP2
LRRC4B
NTRK2
PCDHGC3
SEMA3A
SLITRK2
TPBG
Cell Proliferation
Chromatin
Neuron Projection
Synapse

Fig. 2

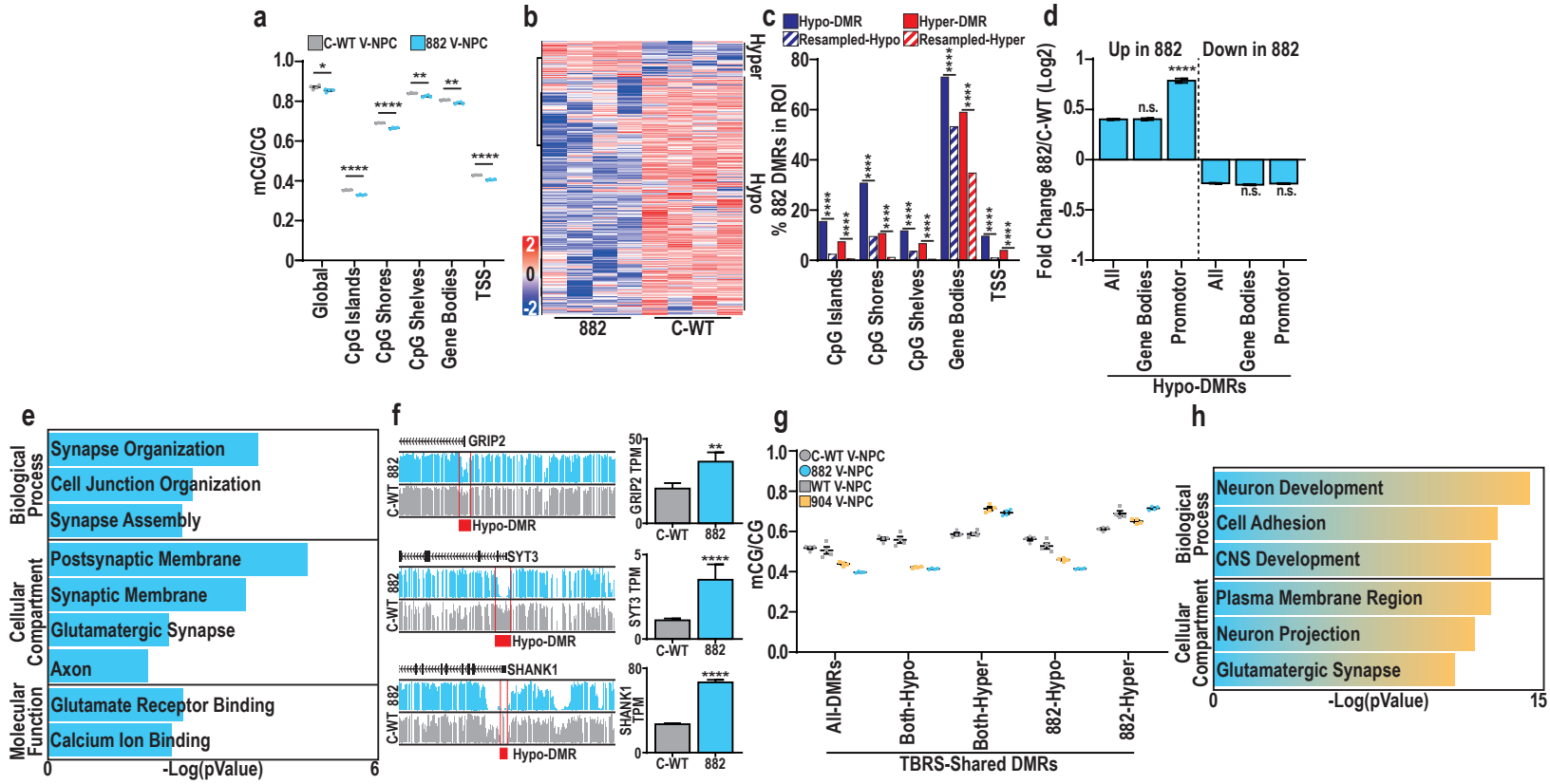
a
C-WT V-NPC
882 V-NPC
mCG/CG
Global
CpG Islands
CpG Shores
CpG Shelves
Gene Bodies
TSS
b
Hyper
Hypo
882
C-WT
c
Hypo-DMR
Hyper-DMR
Resampled-Hypo
Resampled-Hyper
% 882 DMRs in ROI
d
Up in 882
Down in 882
Fold Change 882/C-WT (Log2)
n.s.
All
Gene Bodies
Promotor
Hypo-DMRs
e
Biological Process
Synapse Organization
Cell Junction Organization
Synapse Assembly
Cellular Compartment
Postsynaptic Membrane
Synaptic Membrane
Glutamatergic Synapse
Axon
Molecular Function
Glutamate Receptor Binding
Calcium Ion Binding
-Log(pValue)
f
GRIP2
SYT3
SHANK1
C-WT
882
Hypo-DMR
GRIP2 TPM
SYT3 TPM
SHANK1 TPM
g
C-WT V-NPC
882 V-NPC
WT V-NPC
904 V-NPC
mCG/CG
All-DMRs
Both-Hypo
Both-Hyper
882-Hypo
882-Hyper
TBRS-Shared DMRs
h
Biological Process
Neuron Development
Cell Adhesion
CNS Development
Cellular Compartment
Plasma Membrane Region
Neuron Projection
Glutamatergic Synapse
-Log(pValue)

Fig. 3

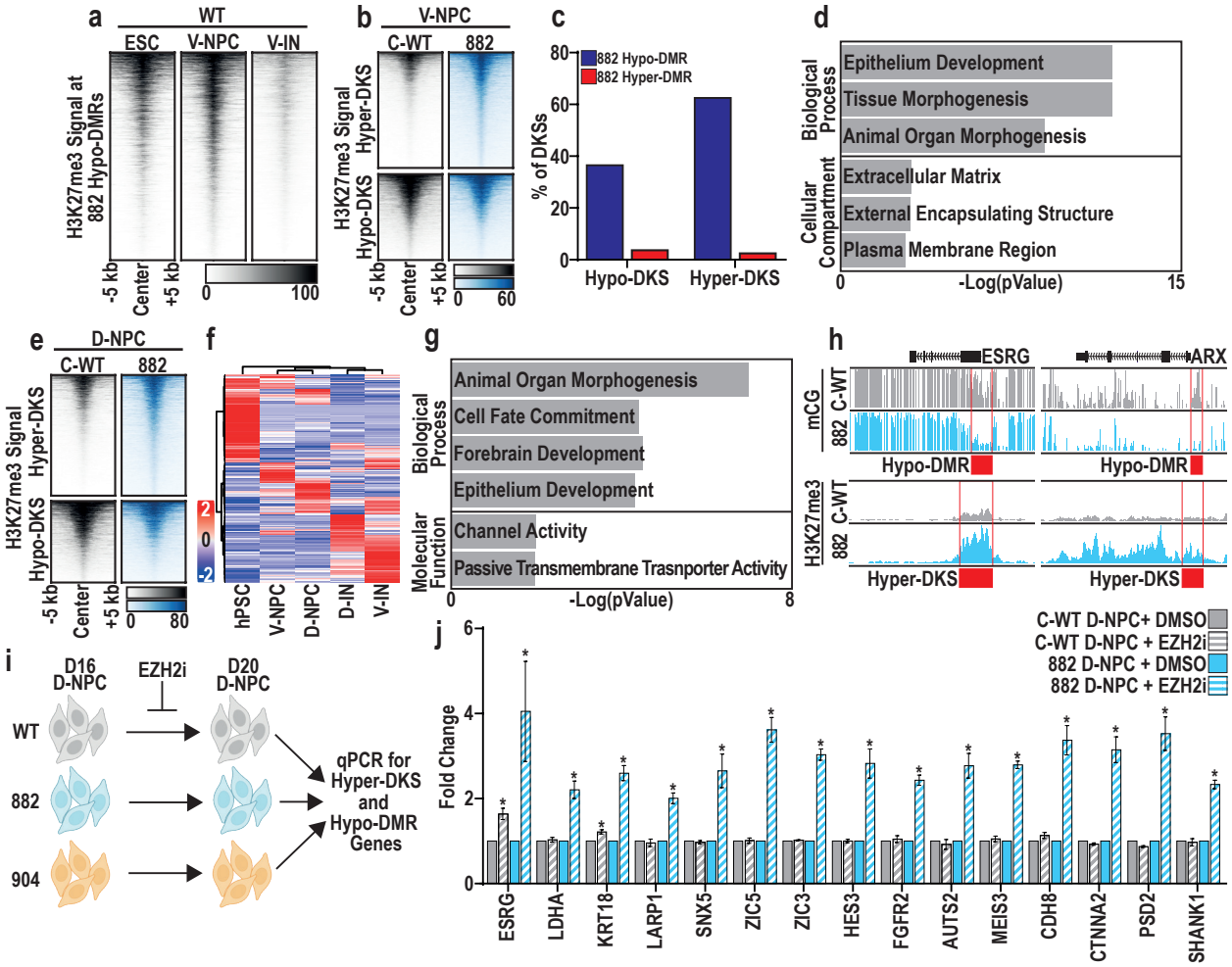
a
WT
ESC
V-NPC
V-IN
H3K27me3 Signal at 882 Hypo-DMRs
-5 kb
Center
+5 kb
0
100
b
V-NPC
C-WT
882
H3K27me3 Signal
Hyper-DKS
Hypo-DKS
-5 kb
Center
+5 kb
0
60
c
882 Hypo-DMR
882 Hyper-DMR
% of DKSs
80
60
40
20
0
Hypo-DKS
Hyper-DKS
d
Biological Process
Epithelium Development
Tissue Morphogenesis
Animal Organ Morphogenesis
Cellular Compartment
Extracellular Matrix
External Encapsulating Structure
Plasma Membrane Region
0
-Log(pValue)
15
e
D-NPC
C-WT
882
H3K27me3 Signal
Hyper-DKS
Hypo-DKS
-5 kb
Center
+5 kb
0
80
f
2
0
-2
hPSC
V-NPC
D-NPC
D-IN
V-IN
g
Biological Process
Animal Organ Morphogenesis
Cell Fate Commitment
Forebrain Development
Epithelium Development
Molecular Function
Channel Activity
Passive Transmembrane Trasnporter Activity
0
-Log(pValue)
8
h
ESRG
ARX
mCG
C-WT
882
Hypo-DMR
Hypo-DMR
H3K27me3
C-WT
882
Hyper-DKS
Hyper-DKS
i
D16 D-NPC
EZH2i
D20 D-NPC
WT
882
904
qPCR for Hyper-DKS and Hypo-DMR Genes
j
C-WT D-NPC+ DMSO
C-WT D-NPC + EZH2i
882 D-NPC + DMSO
882 D-NPC + EZH2i
Fold Change
6
4
2
0
ESRG
LDHA
KRT18
LARP1
SNX5
ZIC5
ZIC3
HES3
FGFR2
AUTS2
MEIS3
CDH8
CTNNA2
PSD2
SHANK1

Fig. 4

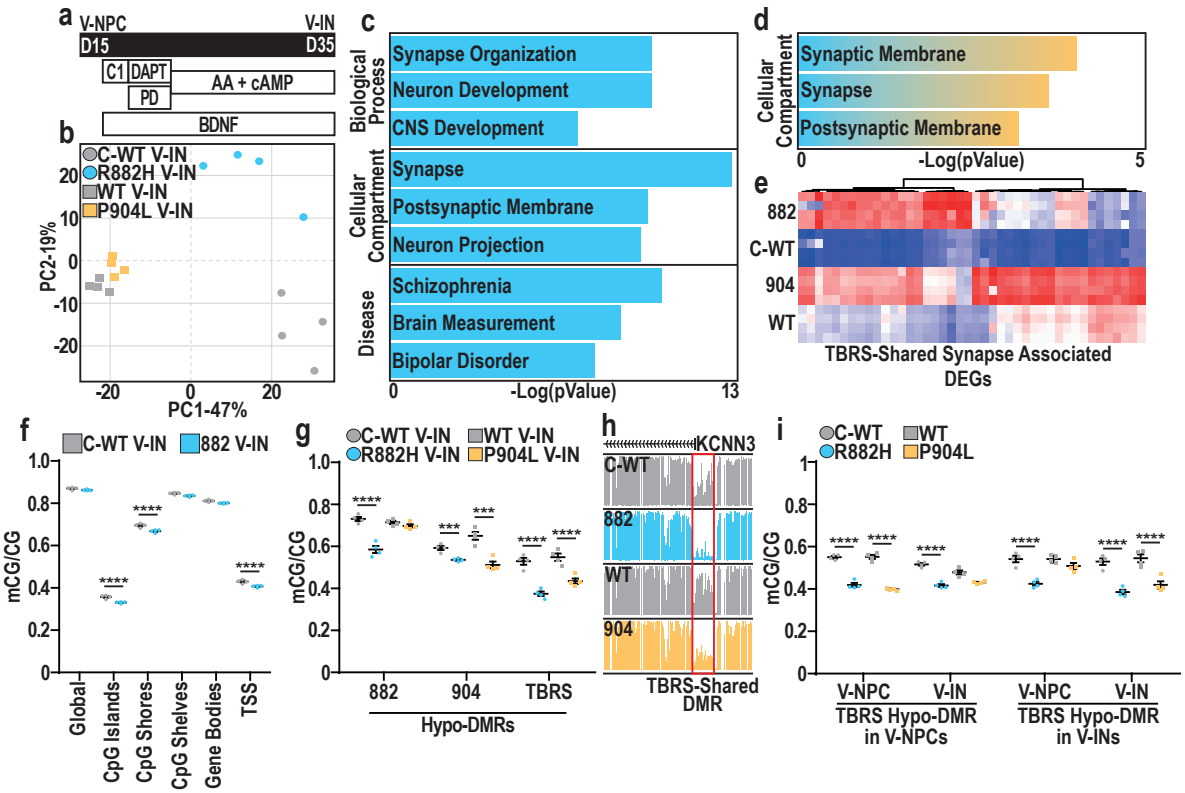
a
V-NPC
V-IN
D15
D35
C1
DAPT
PD
AA + cAMP
BDNF
b
C-WT V-IN
R882H V-IN
WT V-IN
P904L V-IN
PC2-19%
PC1-47%
c
Biological Process
Synapse Organization
Neuron Development
CNS Development
Cellular Compartment
Synapse
Postsynaptic Membrane
Neuron Projection
Disease
Schizophrenia
Brain Measurement
Bipolar Disorder
-Log(pValue)
d
Cellular Compartment
Synaptic Membrane
Synapse
Postsynaptic Membrane
-Log(pValue)
e
882
C-WT
904
WT
TBRS-Shared Synapse Associated DEGs
f
C-WT V-IN
882 V-IN
mCG/CG
Global
CpG Islands
CpG Shores
CpG Shelves
Gene Bodies
TSS
g
C-WT V-IN
WT V-IN
R882H V-IN
P904L V-IN
mCG/CG
882
904
TBRS
Hypo-DMRs
h
KCNN3
C-WT
882
WT
904
TBRS-Shared DMR
i
C-WT
WT
R882H
P904L
mCG/CG
V-NPC
V-IN
TBRS Hypo-DMR in V-NPCs
TBRS Hypo-DMR in V-INs

Fig. 5

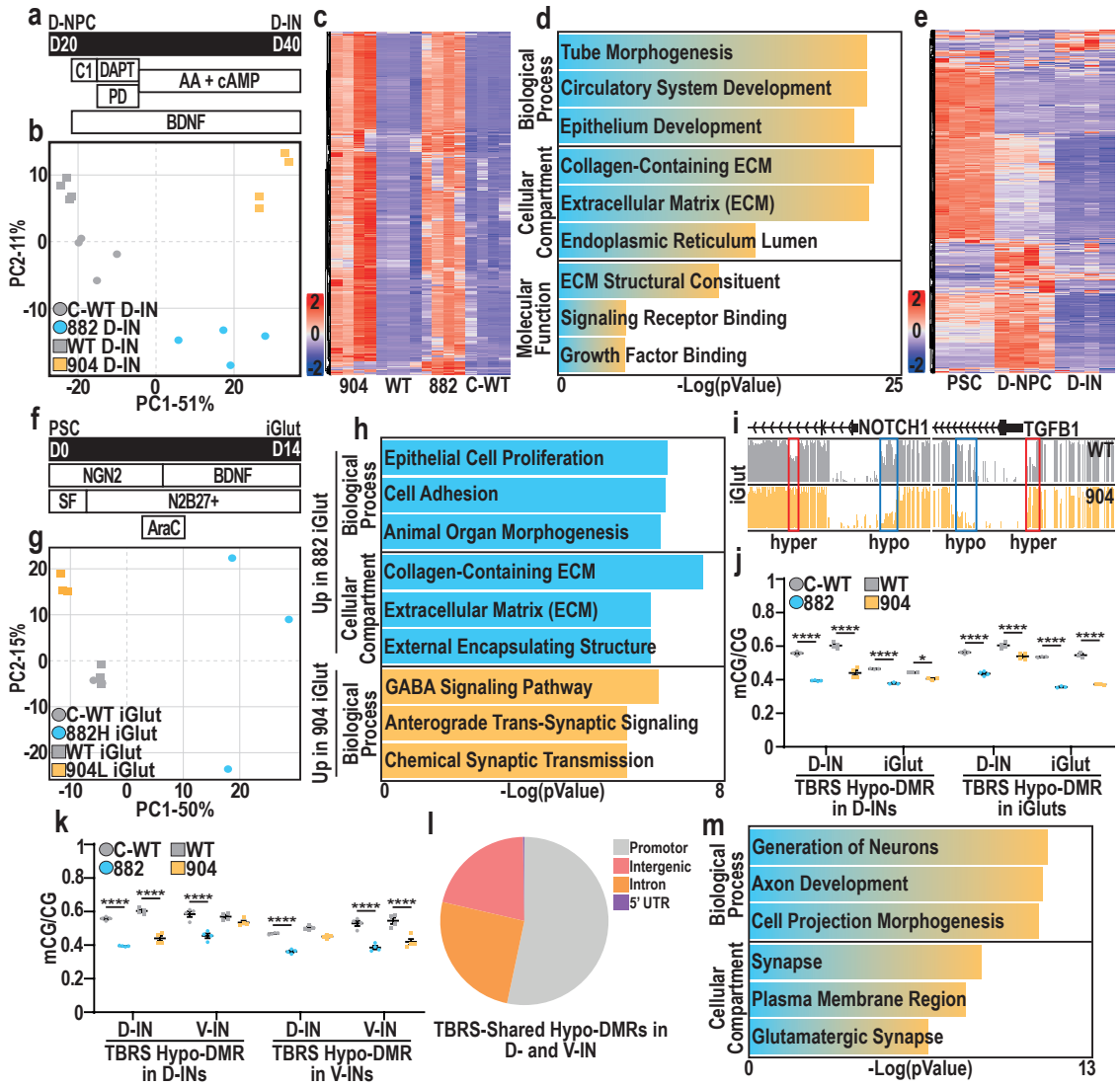
a
D-NPC
D-IN
D20
D40
C1
DAPT
PD
AA + cAMP
BDNF
b
PC2-11%
PC1-51%
C-WT D-IN
882 D-IN
WT D-IN
904 D-IN
c
904
WT
882
C-WT
d
Biological Process
Tube Morphogenesis
Circulatory System Development
Epithelium Development
Cellular Compartment
Collagen-Containing ECM
Extracellular Matrix (ECM)
Endoplasmic Reticulum Lumen
Molecular Function
ECM Structural Consituent
Signaling Receptor Binding
Growth Factor Binding
-Log(pValue)
e
PSC
D-NPC
D-IN
f
PSC
iGlut
D0
D14
NGN2
BDNF
SF
N2B27+
AraC
g
PC2-15%
PC1-50%
C-WT iGlut
882H iGlut
WT iGlut
904L iGlut
h
Up in 882 iGlut
Biological Process
Epithelial Cell Proliferation
Cell Adhesion
Animal Organ Morphogenesis
Cellular Compartment
Collagen-Containing ECM
Extracellular Matrix (ECM)
External Encapsulating Structure
Up in 904 iGlut
Biological Process
GABA Signaling Pathway
Anterograde Trans-Synaptic Signaling
Chemical Synaptic Transmission
-Log(pValue)
i
NOTCH1
TGFB1
iGlut
WT
904
hyper
hypo
hypo
hyper
j
C-WT
882
WT
904
mCG/CG
D-IN
iGlut
TBRS Hypo-DMR in D-INs
TBRS Hypo-DMR in iGluts
k
C-WT
882
WT
904
mCG/CG
D-IN
V-IN
TBRS Hypo-DMR in D-INs
TBRS Hypo-DMR in V-INs
l
Promotor
Intergenic
Intron
5' UTR
TBRS-Shared Hypo-DMRs in D- and V-IN
m
Biological Process
Generation of Neurons
Axon Development
Cell Projection Morphogenesis
Cellular Compartment
Synapse
Plasma Membrane Region
Glutamatergic Synapse
-Log(pValue)

Fig. 6

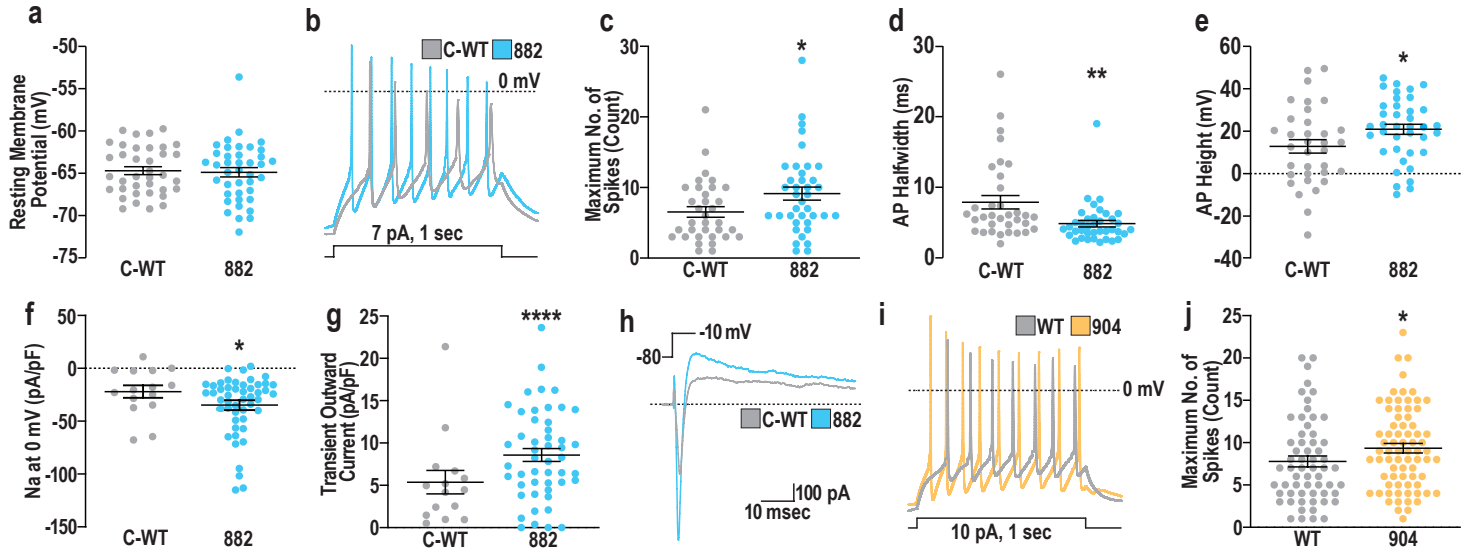
a
Resting Membrane Potential (mV)
-50
-55
-60
-65
-70
-75
C-WT
882
b
C-WT
882
0 mV
7 pA, 1 sec
c
Maximum No. of Spikes (Count)
30
20
10
0
*
C-WT
882
d
AP Halfwidth (ms)
30
20
10
0
**
C-WT
882
e
AP Height (mV)
60
40
20
0
-20
-40
*
C-WT
882
f
Na at 0 mV (pA/pF)
50
0
-50
-100
-150
*
C-WT
882
g
Transient Outward Current (pA/pF)
25
20
15
10
5
0
****
C-WT
882
h
-10 mV
-80
C-WT
882
100 pA
10 msec
i
WT
904
0 mV
10 pA, 1 sec
j
Maximum No. of Spikes (Count)
25
20
15
10
5
0
*
WT
904

Fig. 7

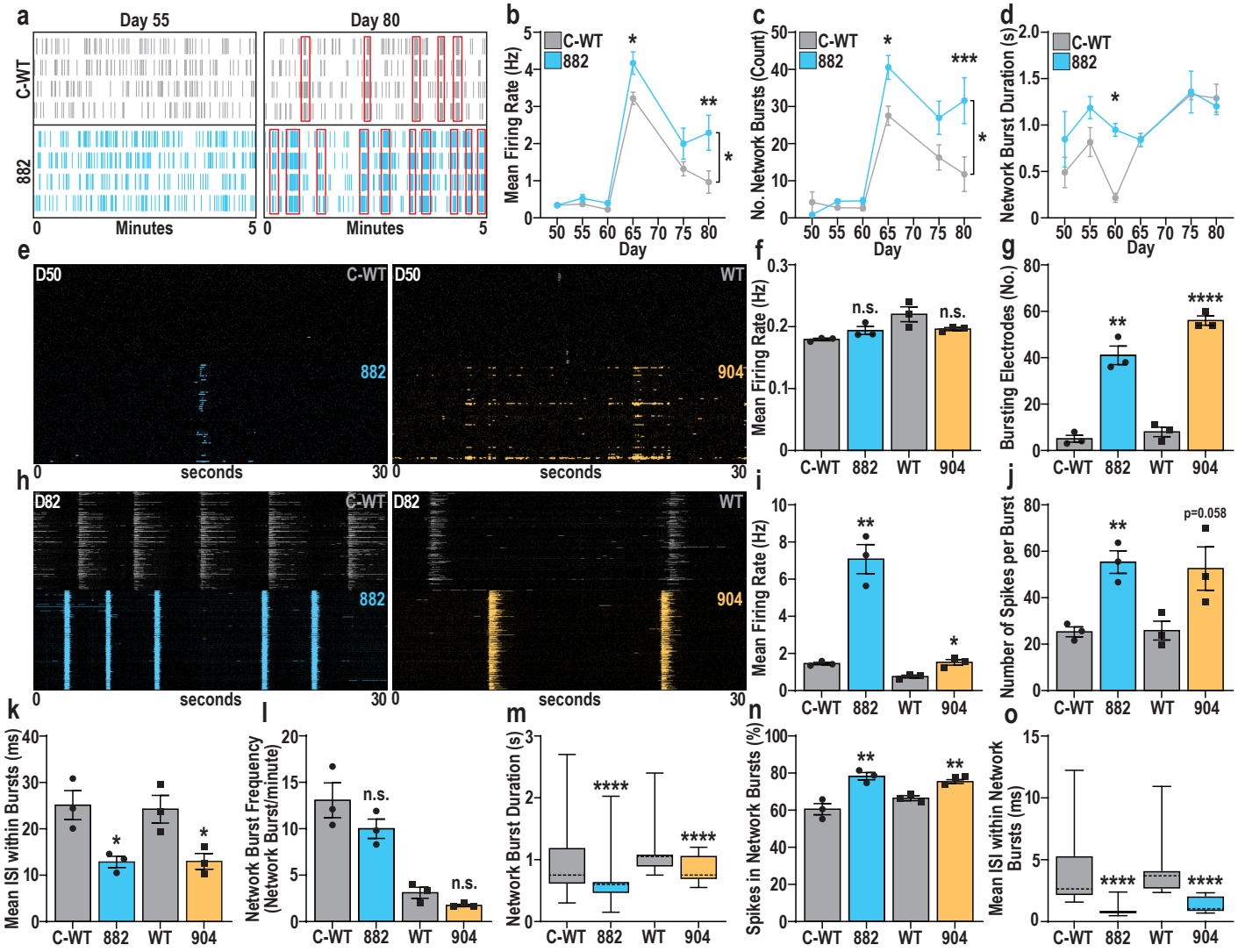
a
Day 55
Day 80
C-WT
882
0
Minutes
5
b
C-WT
882
Mean Firing Rate (Hz)
Day
c
No. Network Bursts (Count)
d
Network Burst Duration (s)
e
D50
C-WT
882
D50
WT
904
seconds
30
f
Mean Firing Rate (Hz)
n.s.
g
Bursting Electrodes (No.)
h
D82
C-WT
882
D82
WT
904
i
Mean Firing Rate (Hz)
j
Number of Spikes per Burst
p=0.058
k
Mean ISI within Bursts (ms)
l
Network Burst Frequency (Network Burst/minute)
m
Network Burst Duration (s)
n
Spikes in Network Bursts (%)
o
Mean ISI within Network Bursts (ms)
C-WT
882
WT
904